




Molecular Gas Structures traced by ¹³CO Emission in the 18,190 ¹²CO Molecular Clouds from the MWISP Survey

LIXIA YUAN ^{1,1}, JI YANG ¹, FUJUN DU ¹, YANG SU ¹, XUNCHUAN LIU ², SHAOBO ZHANG ¹, YAN SUN ¹,
XIN ZHOU ¹, QING-ZENG YAN ¹ AND YUEHUI MA ¹

¹*Purple Mountain Observatory and Key Laboratory of Radio Astronomy, Chinese Academy of Sciences,
10 Yuanhua Road, Qixia District, Nanjing 210033, PR China*

²*Shanghai Astronomical Observatory, Chinese Academy of Sciences, PR China*

ABSTRACT

After the morphological classification of the 18,190 ¹²CO molecular clouds, we further investigate the properties of their internal molecular gas structures traced by the ¹³CO($J = 1-0$) line emissions. Using three different methods to extract the ¹³CO gas structures within each ¹²CO cloud, we find that $\sim 15\%$ of ¹²CO clouds (2851) have ¹³CO gas structures and these ¹²CO clouds contribute about 93% of the total integrated flux of ¹²CO emission. In each of 2851 ¹²CO clouds with ¹³CO gas structures, the ¹³CO emission area generally does not exceed 70% of the ¹²CO emission area, and the ¹³CO integrated flux does not exceed 20% of the ¹²CO integrated flux. We reveal a strong correlation between the velocity-integrated intensities of ¹²CO lines and those of ¹³CO lines in both ¹²CO and ¹³CO emission regions. This indicates the H₂ column densities of molecular clouds are crucial for the ¹³CO lines emission. After linking the ¹³CO structure detection rates of the 18,190 ¹²CO molecular clouds to their morphologies, i.e. nonfilaments and filaments, we find that the ¹³CO gas structures are primarily detected in the ¹²CO clouds with filamentary morphologies. Moreover, these filaments tend to harbor more than one ¹³CO structure. That demonstrates filaments not only have larger spatial scales, but also have more molecular gas structures traced by ¹³CO lines, i.e. the local gas density enhancements. Our results favor the turbulent compression scenario for filament formation, in which dynamical compression of turbulent flows induces the local density enhancements. The nonfilaments tend to be in the low-pressure and quiescent turbulent environments of the diffuse interstellar medium.

Keywords: Interstellar medium(847) — Interstellar molecules(849) — Molecular clouds(1072)

1. INTRODUCTION

Molecular clouds (MCs) are the fundamental forms of the molecular interstellar medium (ISM), which represent its coldest (~ 10 K), densest components ($n > 30$ cm⁻³) of the ISM. However, how molecular clouds form and what mechanisms determine their physical properties are still under debate. Previous studies have proposed several mechanisms, including large-scale gravitational instabilities (Lin & Shu 1964; Goldreich & Lynden-Bell 1965), agglomeration of smaller clouds (Oort 1954; Field & Saslaw 1965; Dobbs & Baba 2014), turbulent flows (Vazquez-Semadeni et al. 1995; Passot et al. 1995; Ballesteros-Paredes et al. 1999a; Vázquez-Semadeni et al. 2006; Heitsch et al. 2006; Koyama & Inutsuka 2002; Beuther et al. 2020). Understanding the mechanism by which molecular clouds form and evolve are crucial for comprehending star formation and galaxy evolution.

Molecular clouds usually present complex and hierarchical structures. Since its discovery by Wilson et al. (1970), CO line emission has been widely used as a tracer of molecular gas. The boundaries of MCs are usually defined by either the low- J rotational CO emission or extinction above some threshold (Heyer & Dame 2015). The unbiased

Galactic plane CO survey, the Milky Way Imaging Scroll Painting (MWISP), is performed using the 13.7m millimeter-wavelength telescope of Purple Mountain Observatory (PMO) and observes ^{12}CO , ^{13}CO , and C^{18}O ($J = 1 - 0$) spectra, simultaneously (Su et al. 2019). The first phase of the MWISP CO project covering the Galactic longitude from $l = 9^\circ.75$ to $230^\circ.25$ and the Galactic latitude from $b = -5^\circ.25$ to $5^\circ.25$, has been completed. The second phase of MWISP has begun and intend to extend the Galactic latitude from $b = -10^\circ.25$ to $10^\circ.25$. This high-quality CO survey provides us with opportunities to promote the analysis of the molecular clouds properties to a large sample spanning wide spatial scales, different evolutionary stages and various environments.

After observations with sufficient sensitivity and high spatial resolution carried out using the Herschel telescope, filaments became known to play an important role in the star formation of MCs (André et al. 2010; Molinari et al. 2010; André et al. 2014, 2016; Yuan et al. 2019, 2020; Peretto et al. 2022). Our researchs in Yuan et al. (2021) (Paper I) use the 18,190 MCs identified by the ^{12}CO lines data from MWISP survey and classified them as filaments and nonfilaments. We found that the filaments make up about 10% of the total number of molecular clouds, while contributing about 90% of the total integrated flux of ^{12}CO line emission. Despite the systematic difference between the filaments and nonfilaments in their spatial areas, their averaged H_2 column densities do not vary significantly. Neralwar et al. (2022a) have classified the SEDIGISM clouds into four morphologies and found that most of molecular clouds present elongated structures. In addition, the ringlike clouds show the peculiar properties, which are speculated to be related to the physical mechanisms that regulate their formation and evolution (Neralwar et al. 2022b). Following our paper I, several questions can be asked, for instance, is there any possible evolution sequence between filaments and nonfilaments? What are the physics behind the molecular clouds presenting filaments or nonfilaments? Quantifying the amount, distribution, and kinematics of the diffuse and dense gas among them may provide new clues to answering these questions.

Compared with the $^{12}\text{CO}(1-0)$ line emission having a critical density of $\sim 10^2 \text{ cm}^{-3}$, the less abundant isotope $^{13}\text{CO}(1-0)$ lines can trace the denser gas with a density of $\sim 10^3 \text{ cm}^{-3}$. The large-scale, unbiased, and highly sensitive data on CO and its isotopic lines from the MWISP survey provides us with opportunities to systematically investigate the spatial distribution and properties of the diffuse and dense molecular gas in a large sample of Molecular clouds.

In this paper, we use the $^{13}\text{CO}(1-0)$ line emission to trace relatively dense gas components within 18,190 ^{12}CO molecular clouds and reveal the relationship between the ^{13}CO gas fractions and morphologies in molecular clouds. In section 2, we describe the data set, including the ^{13}CO line emission data and ^{12}CO molecular cloud catalog; Section 3 introduces three different methods used to extract ^{13}CO molecular gas structures in ^{12}CO molecular clouds and compares their results. In Section 4, we present the distribution of the physical parameters of the extracted ^{13}CO gas structures within the ^{12}CO MCs and systematically investigate the correlation between $^{12}\text{CO}(1-0)$ and $^{13}\text{CO}(1-0)$ line emission in the ^{12}CO clouds having ^{13}CO structures, in addition, we also link the the ^{13}CO gas structures and the morphologies of ^{12}CO molecular clouds to reveal the possible relation between them. Section 5 discusses how our observational results provide the clues for us to understand the molecular clouds' formation and evolution. We conclude with a summary in Section 6.

2. DATA

2.1. $^{13}\text{CO } J = 1 - 0$ data from MWISP survey

The ^{13}CO data is from the MWISP survey, which is an ongoing northern Galactic plane CO survey. This survey is conducted by the 13.7m telescope at Delingha, China. The detailed introductions for the telescope, the multibeam receiver system, observation mode, and data reduction procedures are described in Su et al. (2019). The half-power beamwidth (HPBW) for the telescope at 115 GHz is about $50''$. The velocity separation of ^{13}CO lines is about 0.17 km s^{-1} . The main beam efficiency (η_{MB}) varied between 40% and 50%.

In this work, we focus on the ^{13}CO emission in the Second Galactic Quadrant with $104^\circ.75 < l < 150^\circ.25$, $|b| < 5^\circ.25$, and $-95 \text{ km s}^{-1} < V_{\text{LSR}} < 25 \text{ km s}^{-1}$. Figure 1 presents the large-scale ^{13}CO gas distribution as a velocity-integrated intensity map and a latitude-integrated intensity map.

2.2. Catalog and morphology classification

We define a molecular cloud as a contiguous structure in the position-position-velocity (PPV) data cube with $^{12}\text{CO}(1-0)$ line intensities above a certain threshold. As described in Yan et al. (2021), a total of available 18,190 molecular clouds have been identified from the ^{12}CO data cube in the range of $104^\circ.75 < l < 150^\circ.25$, $|b| < 5^\circ.25$, and $-95 \text{ km s}^{-1} < V_{\text{LSR}} < 25 \text{ km s}^{-1}$.

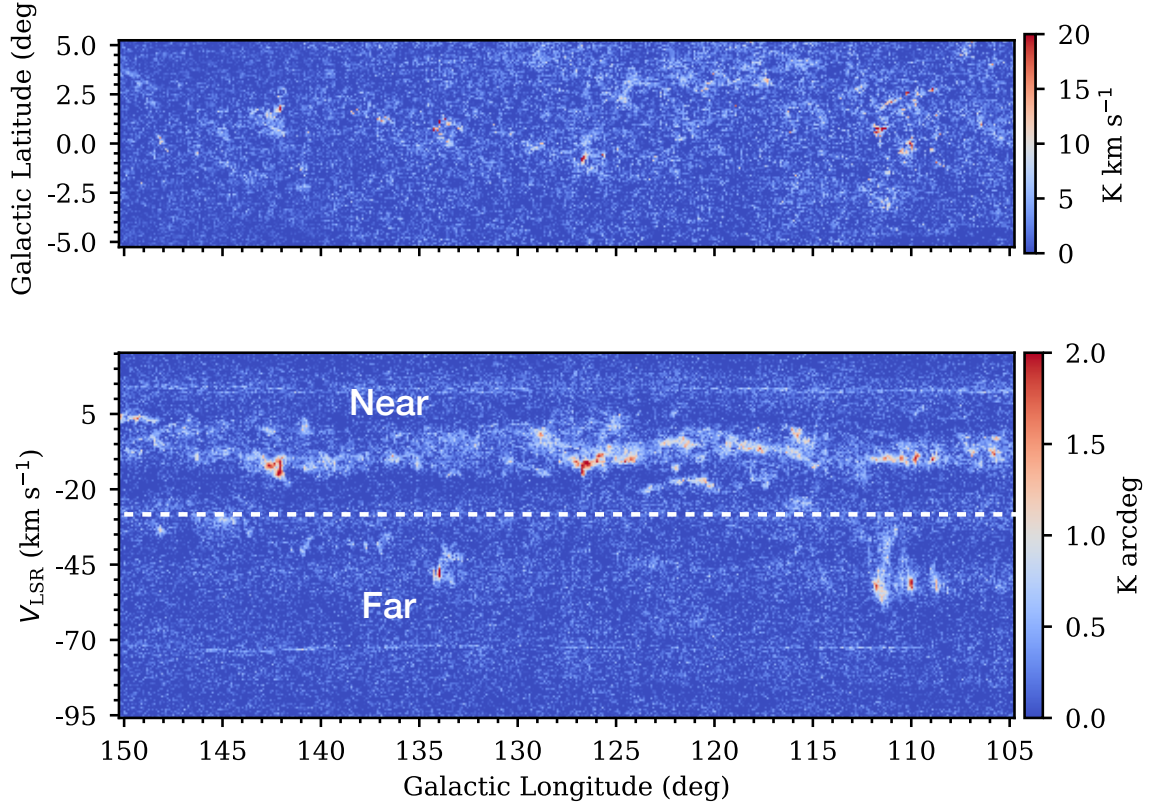


Figure 1. Top Panel: the velocity-integrated intensity map of $^{13}\text{CO}(1-0)$ emission in the second Galactic quadrant with $104.75^\circ < l < 150.25^\circ$ and $|b| < 5.25^\circ$. This map is derived by integrating the ^{13}CO emission over the velocity range between -95 km s^{-1} and 25 km s^{-1} . The distribution of noise RMS for the spectrum in each pixel is presented in Figure A1, the mean noise RMS is about 0.25 K . The sensitivity for this velocity-integrated map can be calculated as $\sigma \times \sqrt{N} \times dv = 1.2 \text{ K km/s}$, where σ is the mean noise RMS (0.25 K), dv represents the velocity resolution, its value is 0.17 km/s , $N = 760$ is the number of the velocity channels. **Bottom Panel:** the latitude-integrated intensity map of $^{13}\text{CO}(1-0)$ emission. This map is derived by integrating the ^{13}CO emission over the latitude range from -5.25° to 5.25° . The white dashed line at $V_{\text{LSR}} = -30 \text{ km s}^{-1}$ divides the molecular clouds into two groups, i.e., the Near and Far groups, as described in Section 4.1. The velocity-integrated intensity maps and the latitude-integrated maps for the ^{13}CO emission in the near and far velocity ranges, are shown in Figure A2 and A3, respectively.

$s^{-1} < V_{\text{LSR}} < 25 \text{ km s}^{-1}$, using the Density-based Spatial Clustering of Applications with Noise (DBSCAN) algorithm (Ester et al. 1996; Yan et al. 2020).

In the paper I, we have completed the morphological classification for these ^{12}CO molecular clouds, which are mainly classified into filaments and nonfilaments (Yuan et al. 2021). In this work, we aim to analyze the properties of high column density gas traced by the ^{13}CO line emission in these molecular cloud samples.

3. EXTRACTING $^{13}\text{CO } J = 1 - 0$ EMISSION STRUCTURES WITHIN ^{12}CO MOLECULAR CLOUDS

In this work, the ^{13}CO emission structures are defined as molecular structures within the ^{12}CO molecular clouds whose spectral voxels have the ^{13}CO line intensities above a certain threshold. We utilize three different methods, i.e. clipping, DBSCAN (Ester et al. 1996; Yan et al. 2020), and moment mask (Dame 2011) to extract the ^{13}CO gas structures.

3.1. Background noise

Before extracting the ^{13}CO line emission within the ^{12}CO molecular clouds, it is necessary to determine their RMS noises (σ). The ^{13}CO spectral line data are chopped into the separate data cubes with sizes equivalent to the extent of ^{12}CO emission in the PPV space for ^{12}CO molecular clouds. Figure 2 presents a sketch map illustrating the distribution

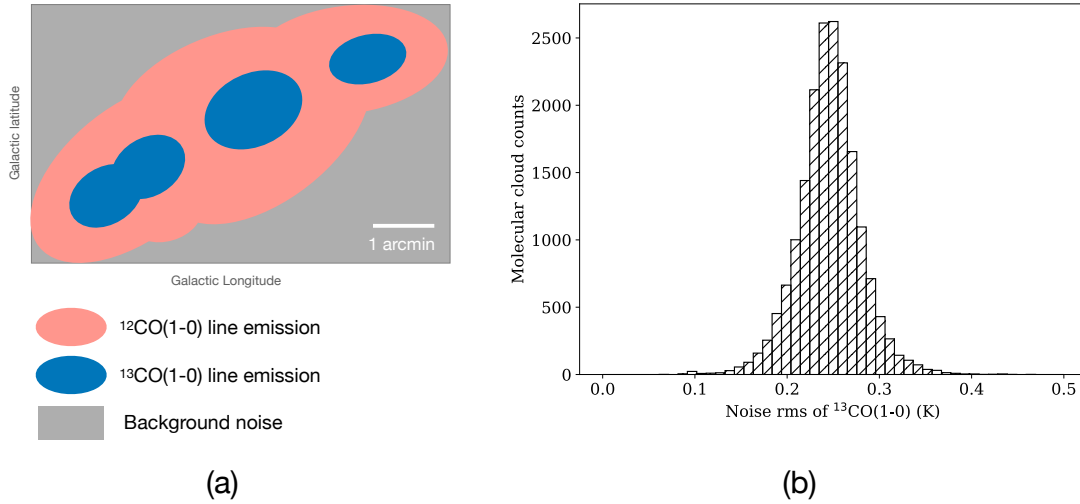


Figure 2. Panel (a): A cartoon demonstrating the distribution of ^{12}CO molecular cloud, ^{13}CO line emission, and the background region for estimating the RMS noise. Panel (b): The distribution of the RMS noise of the ^{13}CO line for each molecular cloud.

of ^{12}CO molecular cloud, the ^{13}CO emission structures, and the background noise in a separate data cube. The voxels within the background region in each ^{13}CO data cube are utilized to estimate the RMS noise of ^{13}CO lines for each molecular cloud. The distribution of the resultant ^{13}CO rms noises for all of 18,190 molecular clouds are presented in Figure 2. The typical value is about 0.25 K. The corresponding RMS noise for each molecular cloud is used for the ^{13}CO emission extraction. Furthermore, the values of voxels in the background region of each ^{13}CO data cube are set to zeros, so that the ^{13}CO structures are extracted within the ^{12}CO emission boundaries. We extract the ^{13}CO emission structures in these chopped 18,190 ^{13}CO data cubes, which are correspond to the 18,190 ^{12}CO molecular clouds.

3.2. Three methods

3.2.1. Clipping

Clipping is a common technique, which directly extracts the structures containing the ^{13}CO spectral channels above the statistical significance level. Spectral channels in each ^{13}CO data cube having intensities above the defined clipping levels are extracted as the significant ^{13}CO emission. Whereas the clipping can not avoid the positive noise spikes with values above the clipping level, unless the clipping level is enough high. The high threshold used may lead to loss of the faint emission with intensities below the cutoff levels.

3.2.2. Moment Mask

The main point of a moment mask is that the ^{13}CO emission is extracted on the smoothed ^{13}CO spectral line data, to reduce the effects of noise spikes. The extracted structures are further extended to the adjacent voxels, whose ranges are determined by the smoothed spatial and velocity resolutions. The MWISP ^{13}CO data has a spatial resolution of ~ 50 arcsec and a velocity resolution of 0.17 km s^{-1} , we smooth the data with two times the beam size ($\text{FWHM}_S \sim 100''$) in position space and with four times the velocity channels in velocity space ($\text{FWHM}_V \sim 0.7 \text{ km s}^{-1}$).

In the smoothed ^{13}CO data, we calculate the noise RMS (σ_{sm}) and extract the ^{13}CO emissions with intensities higher than the defined σ_{sm} levels. After that, the extracted ^{13}CO structures are extended to the structures containing the voxels, which are adjacent to the extracted voxels. The adjacent voxels are defined as the ns pixels in spatially and nv pixels in velocity. Among that, $ns = 0.5 \times \text{FWHM}_S / ds$, $nv = 0.5 \times \text{FWHM}_V / dv$, ds and dv are the spatial and velocity resolutions for the raw data, respectively (Dame 2011). According to the resolutions of the smoothed data, we obtain $ns=1$ and $nv=2$. Thus, a total of $3 \times 3 \times 5$ voxels are determined to be adjacent to an extracted ^{13}CO voxel. Based on the boundaries of enlarged structures, we obtain the determined ^{13}CO structures from the raw ^{13}CO data cube.

3.2.3. DBSCAN

DBSCAN algorithm, which was designed to discover clusters in arbitrary shape (Ester et al. 1996), has been developed to extract a set of contiguous voxels in the PPV space with ^{12}CO emission above a certain threshold as a molecular cloud (Yan et al. 2020). This method is based on both the intensity levels and the connectivity of signals. We utilize the identical parameters to extract the ^{13}CO emission as that used for the ^{12}CO molecular clouds (Yan et al. 2020), except for the post-selection criteria of the peak values. For the ^{12}CO emission, its peak intensity in a ^{12}CO molecular cloud needs to be larger than the intensity of its boundary threshold adding 3σ . Owing to the relatively lower value for the ^{13}CO line intensity, its peak intensity in a ^{13}CO structure is larger than the intensity of its boundary threshold adding the 2σ , where σ is the background noise. The parameters used for the DBSCAN extraction are described in detail in Appendix B. The chopped ^{13}CO data cube without any smoothing procedures is used for identifying the ^{13}CO structures by the DBSCAN algorithm.

3.3. Comparison among different methods

3.3.1. Test on a Case: G139.73

We take a ^{12}CO molecular cloud G139.725-0.507-038.33 (hereafter G139.73) as an sample to compare the performances of the three different methods. In Figure C4 and C5, we present the velocity-integrated intensity maps and the latitude-integrated maps of ^{12}CO and ^{13}CO emission for the G139.73, which are integrated by the chopped data cubes without any clipping. Figure 3 shows the ^{13}CO emission fluxes of the G139.73 extracted by three techniques at the cutoff levels from 2σ to 10σ . We should note the noise σ used by the moment mask is estimated using the smoothed data ($\sigma_{\text{sm}} = 0.05$ K), but that for the DBSCAN and clipping, their background noise σ is calculated using the raw data without any smoothing procedures ($\sigma = 0.27$ K). The distribution of integrated fluxes extracted by the DBSCAN and clipping algorithms have a similar trend and the values steep up from 4σ to 2σ . For the moment mask with the noise σ_{sm} of 0.05 K, its extracted fluxes are higher than that from two other methods at the same cutoff levels. To quantify the contribution of the background noises to the ^{13}CO emission fluxes using the three methods, we

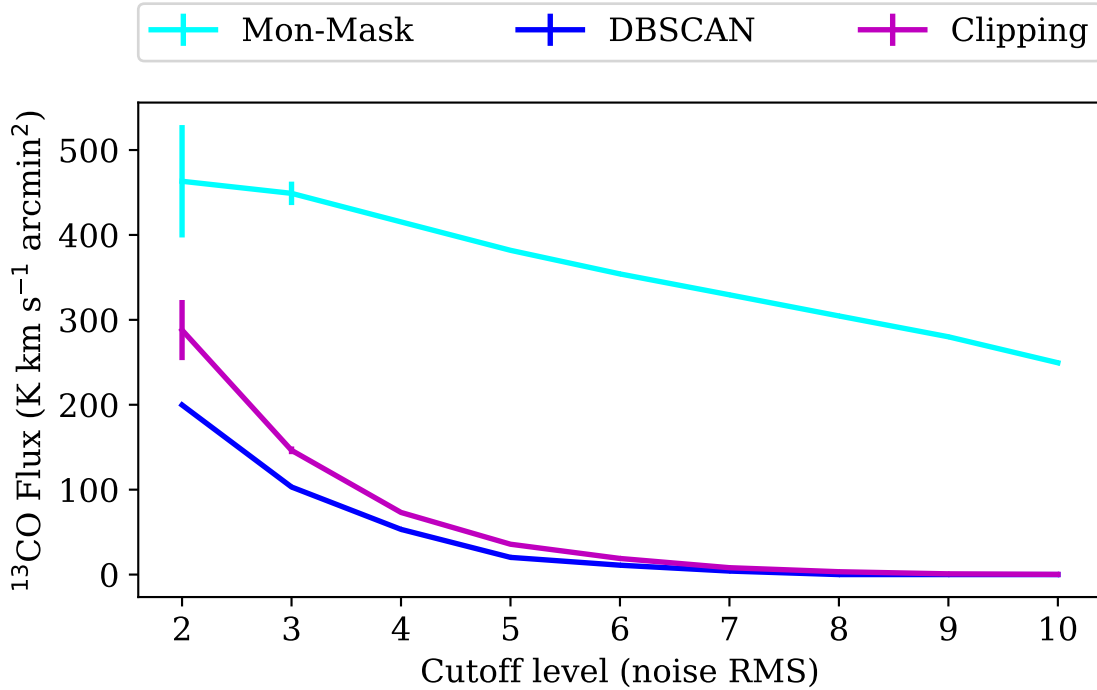


Figure 3. The distribution of ^{13}CO emission fluxes within the ^{12}CO cloud G139.73 extracted by three techniques at the cutoff levels from 2σ to 10σ . The σ for the clipping and DBSCAN is 0.27 K, which is calculated using the raw ^{13}CO line data. Whereas the σ for the moment mask is 0.05 K, estimated from the smoothed ^{13}CO line data.

Table 1. The number detection rates, area ratios, and the total flux ratios between the ^{13}CO and ^{12}CO line emission from three methods.

Methods	Number detection rates	Area ratios	Flux ratios
Clipping	13.5%	10.8%	4.1%
DBSCAN	15.7%	20.3%	6.3%
Moment Mask	15%	20.7%	7.3%

NOTE—The number detection rate is the number of ^{12}CO clouds having ^{13}CO structures divided by the total number of 18,190. The area ratio is the ratio between the total angular areas of the extracted ^{13}CO structures and the total ^{12}CO angular areas of 18,190 ^{12}CO clouds. The flux ratio is the total integrated fluxes of the extracted ^{13}CO line emission divided by that of ^{12}CO line emission.

use a ^{13}CO data cube without the significant ^{13}CO emission to represent the pure background noises. Further, three methods are performed for the extraction of the ^{13}CO line emission in this noise cube at the cutoff levels from 2σ to 10σ . This noise data have the same sizes and spatial positions as that of the G139.73 data cube but in the different radial velocity range of $(-90.3 - 78.4) \text{ km s}^{-1}$. The extracted noise fluxes are shown as the error bars in Figure 3. We find that the background noises contribute about 15% of the integrated fluxes by the moment mask and clipping at the cutoff level of 2σ . Whereas, the DBSCAN almost completely avoids the background noise. We should note that these effects of the background noises on the integrated fluxes are based on a case of G139.73, whose ^{13}CO line emissions have relatively high intensities. For the molecular clouds with faint emission and small spatial scales, the effects of noises can be magnified.

In Figure C6, we present the averaged ^{12}CO and ^{13}CO spectral lines for pixels along the boundaries, which are determined by the clipping at the cutoff level from 2σ to 5σ , as well as the corresponding mean ^{13}CO spectral lines of the extracted ^{13}CO structures. From the cutoff level of 3σ , the averaged ^{13}CO spectrum along the determined boundary begins to have a significant signal. In Figure C7 and C8, we show the velocity-integrated map and latitude-integrated map of the extracted ^{13}CO structures at cutoff level of 3σ and 4σ . We find that there are a lot of positive spikes extracted by the clipping at the cutoff level of 3σ . The same spectral lines for the ^{13}CO structures but extracted using the DBSCAN are presented in Figure C9. For the DBSCAN, the mean ^{13}CO spectrum along its boundary determined at 2σ begins to have a significant ratio of signal to noise (S/N). We also show the integrated maps of the extracted ^{13}CO structures by the DBSCAN at the threshold of 2σ and 3σ in Figure C10 and C11. Figure C12 presents the same ^{13}CO spectral lines for ^{13}CO structures but identified using the moment mask at the cutoff level from $8\sigma_{\text{sm}}$ to $11\sigma_{\text{sm}}$. The averaged-boundary ^{13}CO spectrum begins to show the effective signal at $9\sigma_{\text{sm}}$. The maps for the extracted ^{13}CO structures by the moment mask at $8\sigma_{\text{sm}}$ and $9\sigma_{\text{sm}}$ are shown in Figure C13 and C14. We find that there are tiny ^{13}CO structures extracted by the DBSCAN, not presented in the structures from the moment mask. We should note that the S/N for the averaged-boundary spectrum is related to the number of the spectrum along the boundaries. For the molecular clouds with smaller spatial scales, the averaged-boundary spectrum for ^{13}CO structures extracted using the same method at the same threshold may not have a significant S/N. The cutoff levels of 4σ for the clipping, 2σ for the DBSCAN, and $9\sigma_{\text{sm}}$ for the moment mask are adopted to extract the ^{13}CO structures.

3.3.2. Number detection rate

We determine to extract the ^{13}CO structures within a large sample of ^{12}CO molecular clouds, which have the angular areas spanning from 1 to 10^4 arcmin^2 and the integrated fluxes ranging from ~ 1 to $10^5 \text{ K km s}^{-1} \text{ arcmin}^2$, using the clipping at the cutoff of 4σ , the DBSCAN at the cutoff of 2σ , and the moment mask by a threshold of $9\sigma_{\text{sm}}$, to compare the extracted results from the three different methods.

For the clipping, there are 4,390 molecular clouds detected ^{13}CO line emission. The extracted structure with values above the threshold, whose spatial size is one pixel (0.25 arcmin) or its velocity span is just one channel (0.17 km s^{-1}), is determined as the noise spike. After removing these noise spikes, 2,462 molecular clouds are regarded as having the

significant ^{13}CO line emission. However, the DBSCAN and Moment mask algorithms do not extract individual noise spike. For the DBSCAN algorithm, 2,851 molecular clouds are identified to have the ^{13}CO emission. The moment mask extracts the ^{13}CO line emission in the 2,735 molecular clouds. The number detection rates in the total 18,190 MCs by three methods are listed in Table 1.

3.3.3. Area ratios between the ^{13}CO and ^{12}CO line emission

The total angular area for the 18,190 ^{12}CO molecular clouds is about 228.2 deg^2 . The total angular area for the extracted ^{13}CO structures within the 18,190 ^{12}CO clouds by the clipping is 24.7 deg^2 . The value is 46.2 deg^2 extracted by the DBSCAN and 47.2 deg^2 from the moment mask. The ratios between the total ^{13}CO angular areas of the extracted ^{13}CO structures and the total ^{12}CO angular areas of the 18,190 ^{12}CO clouds are listed in Table 1.

3.3.4. Integrated flux ratios between the ^{13}CO and ^{12}CO line emission

The total $^{12}\text{CO}(1-0)$ emission fluxes for the 18,190 ^{12}CO molecular clouds is $3.7 \times 10^6 \text{ K km s}^{-1} \text{ arcmin}^2$. The total extracted $^{13}\text{CO}(1-0)$ emission flux in this catalog is $1.5 \times 10^5 \text{ K km s}^{-1} \text{ arcmin}^2$ by the clipping. The value is $2.3 \times 10^5 \text{ K km s}^{-1} \text{ arcmin}^2$ by the DBSCAN algorithm and $2.7 \times 10^5 \text{ K km s}^{-1} \text{ arcmin}^2$ by the moment mask method. These total integrated flux ratios between the ^{13}CO and ^{12}CO line emission by three methods are listed in Table 1.

We find that the number detection rates of the DBSCAN and moment mask are consistent with $\sim 15\%$, the value of the clipping is about 2% lower than that of the other two techniques. In addition, the clipping extracts plenty of positive noise spikes. For the total angular areas of the extracted ^{13}CO structures, the values from the clipping is about 50% of that from the DBSCAN and moment mask. For the extracted integrated fluxes of ^{13}CO line emission, the values from the clipping are about 60% of that from the DBSCAN or Moment mask. That indicates the clipping method extracts amounts of noise spikes with intensities larger than the threshold of 4σ , meanwhile, it also loses substantial faint ^{13}CO emission. For either the total angular areas or the total integrated fluxes of the extracted ^{13}CO structures, the values from the moment mask are a bit higher than that from the DBSCAN, while the number detection rate of the moment mask is a bit lower than that from the DBSCAN. Overall, these values from the DBSCAN and moment mask are close.

3.3.5. Differences of extracted basic parameters

The ^{13}CO emissions are extracted within the ^{12}CO clouds by three methods. All the ^{13}CO emissions within the boundary of a ^{12}CO cloud belong to the same cloud. We take all the ^{13}CO line emissions within a ^{12}CO cloud as a whole, referred to as ^{13}CO molecular gas structures. The equivalent angular area of ^{13}CO molecular structures ($\mathcal{A}_{13\text{CO}}$) for a ^{12}CO cloud is the sum of the pixel areas of the extracted ^{13}CO emission regions projected in the l-b panel. The mean velocity span of ^{13}CO molecular structures ($V_{\text{aver},13\text{CO}}$) within a ^{12}CO cloud is the averaged extracted velocity span of each pixel in the ^{13}CO emission regions, weighting by its corresponding velocity-integrated intensity, i.e. $V_{\text{aver},13\text{CO}} = \Sigma(V_{\text{span}}(l, b) \times W_{13\text{CO}}(l, b)) / \Sigma W_{13\text{CO}}(l, b)$. The total ^{13}CO integrated flux ($F_{13\text{CO}}$) is the integrated flux of all the ^{13}CO structures in an individual molecular cloud, $F_{13\text{CO}} = \int T_{\text{mb}}(l, b, v) dl db dv = 0.166 \times 0.25 \Sigma T_{\text{mb}}(l, b, v) \text{ K km s}^{-1} \text{ arcmin}^2$, where $T_{\text{mb}}(l, b, v)$ is the ^{13}CO line intensity at the coordinate of (l, b, v) in PPV space, $dv = 0.166 \text{ km s}^{-1}$ is the velocity resolution. The peak value ($T_{\text{peak},13\text{CO}}$) is the maximal value of the ^{13}CO line intensities for the extracted ^{13}CO structures.

The number distributions of angular sizes ($\mathcal{A}_{13\text{CO}}$), mean velocity spans ($V_{\text{aver},13\text{CO}}$), integrated fluxes ($F_{13\text{CO}}$), and peak intensities ($T_{\text{peak},13\text{CO}}$) of ^{13}CO structures, which are identified by three techniques, are presented in Figure 4. We find the angular sizes of ^{13}CO structures extracted by the clipping are systematically smaller than that from the DBSCAN and moment mask. We compare the angular sizes of ^{13}CO structures from the DBSCAN and moment mask, their distributions in the range of the angular sizes larger than 6 arcmin^2 are similar. There are more structures from the DBSCAN in the range of $1 - 6 \text{ arcmin}^2$. To check the reliability of these extra structures, which are identified by the DBSCAN, but not by the moment mask, we present their ^{13}CO line intensity maps integrated along with three different directions (l, b, v) and their averaged ^{13}CO line spectra. As shown in Figure D15, we find that these structures usually are located around the regions contoured at the levels of half of the peak velocity-integrated intensity of ^{12}CO emission. In addition, their ^{13}CO spectral profiles usually present the Gaussian-like profiles. Thus, we determine these ^{13}CO structures are valid. The number distributions of $T_{\text{peak},13\text{CO}}$ of ^{13}CO line emission from the three techniques are similar in the range of $T_{\text{peak},13\text{CO}} > 2.0 \text{ K}$. After the smooth procedure, a portion of tiny structures with $T_{\text{peak},13\text{CO}} < 2.0 \text{ K}$ may be missed by the moment mask. For the distribution of the mean velocity span of ^{13}CO structures, we find the values from the moment mask tend to be larger than that from the DBSCAN, and the values from the DBSCAN

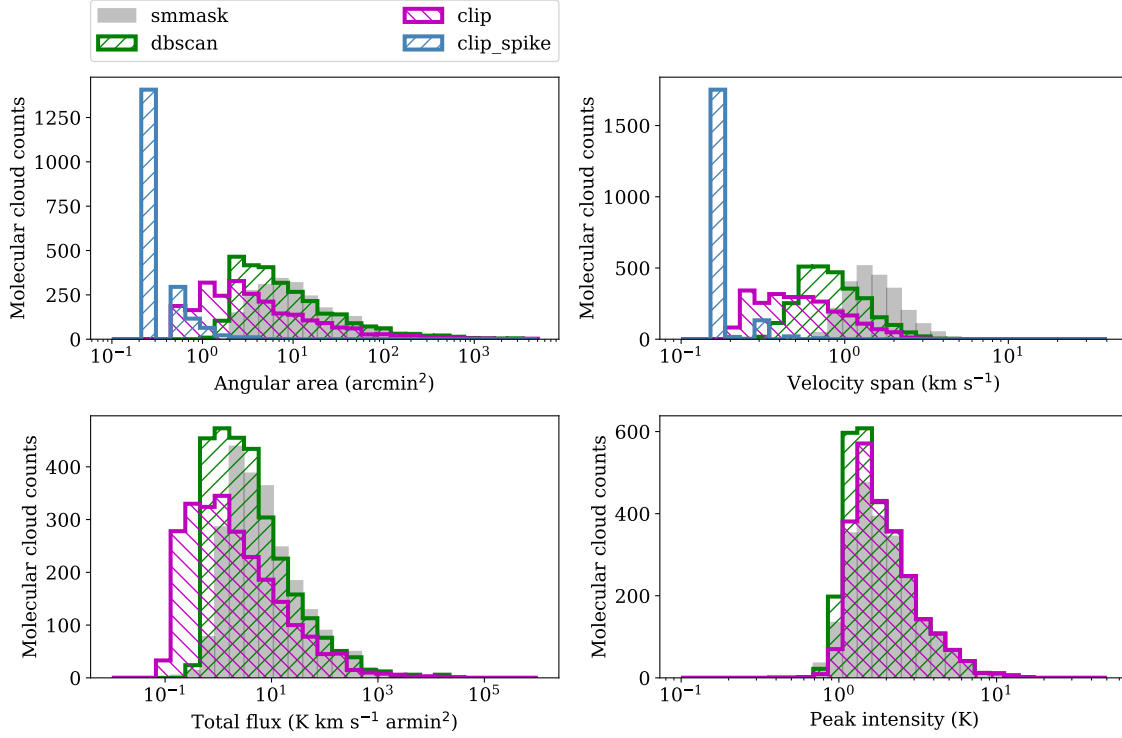


Figure 4. The number distributions of angular sizes, mean velocity spans, the integrated fluxes of ^{13}CO line emission, and the peak intensities of $^{13}\text{CO}(1-0)$ line emission for the ^{13}CO structures extracted by three techniques. For the clipping, the extracted ^{13}CO emission structures with a pixel in spatial scale or a velocity channel in velocity, are determined as the noise spikes and shown as blue histograms.

are prone to be larger than that from the clipping. That may be due to that the extracted voxels in the smoothed data by the moment mask are further extended to the adjacent voxels, while the intensities of voxels extracted by the DBSCAN are larger than 2σ , and the ^{13}CO structures from the clipping only contain the velocity channels with intensities larger than 4σ . Thus the velocity span of ^{13}CO emission in each spatial pixel is derived from the velocity channels with intensities larger than 2σ for the DBSCAN and 4σ for the clipping. The number distributions of $F_{^{13}\text{CO}}$ have a similar trend with that of $\mathcal{A}_{^{13}\text{CO}}$. That means the differences of the $F_{^{13}\text{CO}}$ distributions from three techniques are mainly attributed to their $\mathcal{A}_{^{13}\text{CO}}$ distributions.

3.4. Summary of methods

Above all, the clipping extracts plenty of noise spikes with values larger than 4σ and meanwhile loses the faint significant emission having intensities less than 4σ . That leads to the extracted parameters being systematically smaller than that from the other two methods. In addition, the moment mask leaves out a part of faint and tiny ^{13}CO structures, owing to the smooth procedure. The moment mask is more suitable for the structures with relative large angular sizes and high emission intensities. The DBSCAN algorithm can not only avoid the noise spikes but also preserve the faint and tiny ^{13}CO structures not identified by the moment mask. Each voxel in the PPV space of the structures extracted by the DBSCAN is larger than 2σ . We take the resultant ^{13}CO structures from the DBSCAN, which is consistent with the extraction algorithm used for the ^{12}CO clouds identification, for the follow-up analysis.

Table 2. A catalog of ^{13}CO line emission parameters

Name	l_{cen} (degree)	b_{cen} (degree)	V_{LSR} (km s^{-1})	$\mathcal{A}_{12\text{CO}}$ (arcmin^2)	$V_{\text{span}, 12\text{CO}}$ km s^{-1}	$T_{\text{peak}, 12\text{CO}}$ (K)	$F_{12\text{CO}}$ ($\text{K km s}^{-1} \text{ arcmin}^2$)	$\mathcal{A}_{13\text{CO}}$ (arcmin^2)	$V_{\text{span}, 13\text{CO}}$ km s^{-1}	$T_{\text{peak}, 13\text{CO}}$ (K)	$F_{13\text{CO}}$ ($\text{K km s}^{-1} \text{ arcmin}^2$)
(1)	(2)	(3)	(4)	(5)	(6)	(7)	(8)	(9)	(10)	(11)	(12)
G104.794+02.286-063.40	104.794	02.286	-63.40	03.50	01.67	2.95	4.40	01.50	01.16	0.99	0.55
G104.803-02.869-004.14	104.803	-2.869	-4.14	17.75	02.67	5.30	40.34	04.00	01.00	1.26	1.15
G104.810+01.058-009.45	104.810	01.058	-9.45	12.50	03.51	4.55	20.54	04.00	01.00	1.72	2.09
G104.822-02.335-034.52	104.822	-2.335	-34.52	11.75	04.01	5.14	38.85	02.75	01.33	1.11	0.70
G104.870-00.447-009.32	104.870	-0.447	-9.32	42.25	05.68	6.70	131.49	07.25	01.33	1.44	2.80
G104.871+00.646-001.89	104.871	00.646	-1.89	46.00	02.67	5.59	86.97	02.50	01.00	1.01	0.63
G104.872+01.008-049.95	104.872	01.008	-49.95	33.25	04.84	4.40	68.78	04.25	01.66	1.18	1.83
G104.886+00.134-010.58	104.886	00.134	-10.58	28.25	03.51	8.71	86.43	04.00	01.16	1.47	1.50
G104.923-03.111-046.89	104.923	-3.111	-46.89	04.25	02.00	6.59	9.49	02.00	00.83	1.50	0.88
G104.935+04.396-044.62	104.935	04.396	-44.62	07.25	02.34	5.90	16.76	03.50	01.16	1.40	1.48
G104.980+00.900-055.53	104.980	00.900	-55.53	19.50	03.51	4.43	30.89	02.50	00.83	1.10	0.62
G104.983-02.680-042.49	104.983	-2.680	-42.49	60.75	06.68	5.95	185.27	03.25	01.83	1.32	1.69
G104.997-02.669-004.75	104.997	-2.669	-4.75	26.25	04.34	6.56	79.88	07.25	01.66	1.69	2.78
G105.023+00.538-049.82	105.023	00.538	-49.82	44.25	04.51	6.06	159.96	19.25	01.83	2.61	14.01

NOTE—The central Galactic coordinates (l_{cen} , b_{cen}) for each ^{12}CO cloud are the averaged Galactic coordinates in its velocity-integrated $^{12}\text{CO}(1-0)$ intensity map, weighting by the value of the velocity-integrated $^{12}\text{CO}(1-0)$ intensity. The central velocity (V_{LSR}) for each cloud is the averaged radial velocity in its radial velocity field, weighting by the value of the velocity-integrated $^{12}\text{CO}(1-0)$ intensity. The $\mathcal{A}_{12\text{CO}}$ and $\mathcal{A}_{13\text{CO}}$ are the angular areas of $^{12}\text{CO}(1-0)$ and $^{13}\text{CO}(1-0)$ lines emission, respectively. The $V_{\text{span}, 12\text{CO}}$ represents the velocity span of each cloud cube in the velocity axis of PPV space, which is calculated using the number of velocity channels in the ^{12}CO cloud cube multiplied by a velocity resolution of 0.167 km s^{-1} . The $V_{\text{span}, 13\text{CO}}$ is the velocity range between the maximal and minimal velocity for all the extracted ^{13}CO gas structures within each ^{12}CO molecular cloud. The $T_{\text{peak}, 12\text{CO}}$ and $T_{\text{peak}, 13\text{CO}}$ represent the peak values of $^{12}\text{CO}(1-0)$ and $^{13}\text{CO}(1-0)$ line intensity in each cloud, respectively. The $F_{12\text{CO}}$ is the integrated flux of $^{12}\text{CO}(1-0)$ line emission for each cloud, $F_{12\text{CO}} = \int T_{\text{mb}}(l, b, v) dl db dv = 0.167 \times 0.25 \Sigma T_{\text{mb}}(l, b, v) \text{ K km s}^{-1} \text{ arcmin}^2$, where $T_{\text{mb}}(l, b, v)$ is the ^{12}CO line intensity at the coordinate of (l, b, v) in PPV space, $dv = 0.167 \text{ km s}^{-1}$ is the velocity resolution, $dl db = 0.5 \text{ arcmin} \times 0.5 \text{ arcmin} = 0.25 \text{ arcmin}^2$, the angular size of a pixel is 0.5 arcmin . The $F_{13\text{CO}}$ is calculated using the $^{13}\text{CO}(1-0)$ line emission within each cloud through the same formula, but $T_{\text{mb}}(l, b, v)$ is the ^{13}CO line intensity. This table is available in its entirety from the online journal. A portion is shown here for guidance regarding its form and content.

4. RESULTS

4.1. Comparing the physical properties of molecular clouds with and without ^{13}CO molecular structures

The whole catalog of 18,190 molecular clouds is identified using the $^{12}\text{CO}(1-0)$ line data by the DBSCAN algorithm (Yan et al. 2021). Among that, the 2,851 ^{12}CO clouds have ^{13}CO structures, which are also extracted by the DBSCAN algorithm. Since the boundary of a molecular cloud is defined by the 3D surface of $^{12}\text{CO}(1-0)$ line emission in the PPV space, all the ^{13}CO emissions within this surface belong to the same ^{12}CO cloud. Thus its internal ^{13}CO emission components are characterized as its substructures, which are referred to as ^{13}CO molecular structures. **All the extracted $^{12}\text{CO}(1-0)$ line emission data of 18,190 molecular clouds and the extracted $^{13}\text{CO}(1-0)$ line emission data within the 2,851 ^{12}CO clouds have been published in ScienceDB (Yuan et al. 2022).**

We should note that a single molecular cloud may have more than one individual ^{13}CO molecular structure. We take all the separate ^{13}CO molecular structures in a single ^{12}CO molecular cloud as a unity. The ^{13}CO emission parameters are derived from all the ^{13}CO structures in a ^{12}CO cloud as a whole. The equivalent angular area of ^{13}CO molecular structures for a ^{12}CO cloud is the sum of the pixel areas of the extracted ^{13}CO emission regions projected in the l-b panel. The velocity span of ^{13}CO molecular structures within a ^{12}CO cloud is the range between the maximal and minimal velocity of the extracted ^{13}CO structures along the velocity axis. For a ^{12}CO cloud with multiple ^{13}CO structures, the minimal velocity is the minimal value in the velocity ranges for all the extracted ^{13}CO structures and the maximal velocity is the maximal value of that. Figure C9 illustrates the velocity span for the extracted ^{13}CO structures in the ^{12}CO cloud G139.73. The ^{13}CO integrated fluxes are the integrated fluxes of all the ^{13}CO structures in an individual molecular cloud. The peak value is the maximal value of the ^{13}CO line intensities within the boundary of a ^{12}CO MC. The parameters of ^{13}CO molecular structures for the 2,851 ^{12}CO molecular clouds are listed in Table 2. The rest 15,339 ^{12}CO molecular clouds do not have the significant ^{13}CO structures. We systematically compare the basic physical parameters of the ^{12}CO molecular clouds having ^{13}CO structures (^{13}CO -detects) to that of molecular clouds without ^{13}CO structures (Non ^{13}CO -detects).

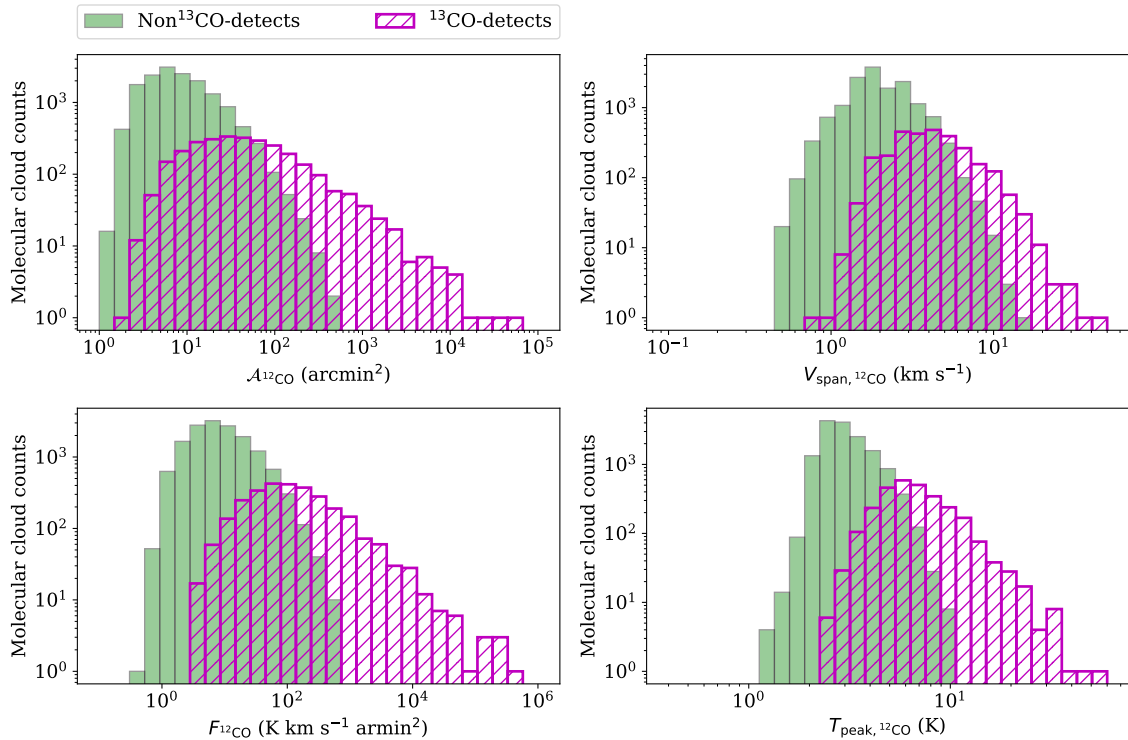


Figure 5. The number distributions of angular areas ($A_{12\text{CO}}$), velocity spans ($V_{\text{span}, 12\text{CO}}$), the peak intensities ($T_{\text{peak}, 12\text{CO}}$) and the integrated fluxes ($F_{12\text{CO}}$) of ^{12}CO line emission for ^{12}CO molecular clouds with and without ^{13}CO structures. The green histograms represent ^{12}CO molecular clouds not having the ^{13}CO structures (Non ^{13}CO -detects). The magenta ones are the ^{12}CO molecular clouds having the ^{13}CO structures (^{13}CO -detects).

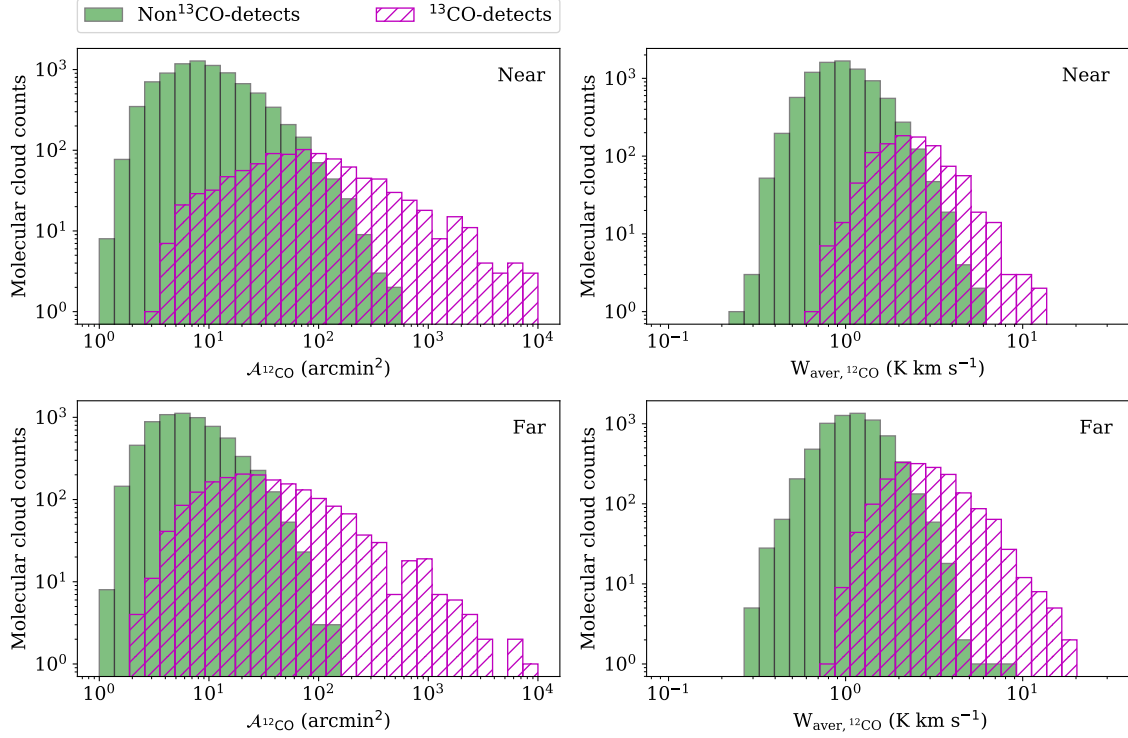


Figure 6. The number distributions of angular areas ($\mathcal{A}_{12\text{CO}}$) and the averaged velocity-integrated intensities ($W_{\text{aver}, 12\text{CO}}$) of ^{12}CO line emission for ^{12}CO molecular clouds in near and far groups, respectively. The near ^{12}CO clouds are in a velocity range of $(-30\ 25)\ \text{km s}^{-1}$, the far ^{12}CO clouds are in $(-95\ -30)\ \text{km s}^{-1}$. The green histograms represent ^{12}CO molecular clouds not having the ^{13}CO structures (Non ^{13}CO -detects). The magenta ones are the ^{12}CO molecular clouds having the ^{13}CO structures (^{13}CO -detects).

In Figure 5, we present the number distributions of angular areas ($\mathcal{A}_{12\text{CO}}$), velocity spans ($V_{\text{span}, 12\text{CO}}$), peak intensities ($I_{\text{peak}, 12\text{CO}}$), and integrated fluxes ($F_{12\text{CO}}$) of ^{12}CO line emission for the ^{13}CO -detects and Non ^{13}CO -detects, respectively. The quantiles at 0.05, 0.25, 0.5, 0.75, and 0.95 of these parameters for the ^{13}CO -detects and Non ^{13}CO -detects are listed in Table 3, respectively. We find that these quantiles of the parameters in the ^{13}CO -detects are systematically larger than that from the Non ^{13}CO -detects. We calculate the total $F_{12\text{CO}}$ of the whole Non ^{13}CO -detects. The value is about $2.5 \times 10^5\ \text{K km s}^{-1}\ \text{arcmin}^2$, which makes up about 6.8% of that of the total 18,190 ^{12}CO molecular clouds ($3.7 \times 10^6\ \text{K km s}^{-1}\ \text{arcmin}^2$). The rest $\sim 93\%$ are from the ^{13}CO -detects. That indicates the ^{13}CO -detects are the main contributor of ^{12}CO emission fluxes, although their number only take a percentage of $\sim 15\%$ in the total number. The total $\mathcal{A}_{12\text{CO}}$ for the 18,190 ^{12}CO clouds is about $228.2\ \text{deg}^2$. Among that, the sum of the $\mathcal{A}_{12\text{CO}}$ from the ^{13}CO -detects take a percentage of 76.2% and that from the Non ^{13}CO -detects take about the rest of 23.8%.

Following the paper I (Yuan et al. 2021), the ^{12}CO clouds are divided into two groups by a V_{LSR} threshold of $-30\ \text{km s}^{-1}$, shown as a white-dashed line in Figure 1. The ^{12}CO clouds with central velocities in a range of $(-30\ 25)\ \text{km s}^{-1}$ are in the near group, and the ^{12}CO clouds with central velocities ranging from $-95\ \text{km s}^{-1}$ to $-30\ \text{km s}^{-1}$ are in the far group. In the near group, there are 9,544 ^{12}CO molecular clouds, among which the ^{13}CO -detects take a percentage of 10.4%. In the far group, there are 8,646 ^{12}CO molecular clouds and 21.5% of them have ^{13}CO structures.

The number detection rate of the ^{13}CO -detects in the near is lower than that in the far group. That may be due to that there are more MCs with faint ^{12}CO emission, but no ^{13}CO emission detected in the near group. The number distributions of the $\mathcal{A}_{12\text{CO}}$ of ^{13}CO -detects and Non ^{13}CO -detects in the near and far group are presented in Figure 6, respectively. The quantiles at 0.05, 0.25, 0.5, 0.75, and 0.95 of their $\mathcal{A}_{12\text{CO}}$ values are listed in Table 4. According

Table 3. The physical parameters of ^{12}CO line emission for Non ^{13}CO -detects and ^{13}CO -detects

Types	Quantile	$\mathcal{A}_{12\text{CO}}$ (arcmin ²)	$V_{\text{span}, 12\text{CO}}$ (km s ⁻¹)	$T_{\text{peak}, 12\text{CO}}$ (K)	$F_{12\text{CO}}$ (K km s ⁻¹ arcmin ²)
Non ^{13}CO -detects	0.05	2.5	1.0	2.2	1.7
	0.25	4.25	1.5	2.5	3.9
	0.5	7.25	2.0	2.9	7.6
	0.75	13.75	2.67	3.5	16.6
	0.95	39.5	4.2	5.0	58.8
	Mean	12.8	2.2	3.1	16.5
^{13}CO -detects	0.05	6.25	1.84	3.8	11.8
	0.25	16.4	2.84	5.1	38.9
	0.5	39	4.0	6.3	101.2
	0.75	102.5	5.68	8.3	299.4
	0.95	640.0	10.35	13.3	2422.3
	Mean	219.5	4.73	7.3	1211.9

NOTE—The quantiles at 0.05, 0.25, 0.5, 0.75 and 0.95 for each parameter in its sequential data and its mean value.

Table 4. The angular areas ($\mathcal{A}_{12\text{CO}}$) and H_2 column densities (N_{H_2}) for ^{13}CO -detects and Non ^{13}CO -detects, which are in the near and far groups, respectively.

Types	Quantile	$\mathcal{A}_{12\text{CO}}$ (arcmin ²)	N_{H_2} 10 ²⁰ cm ⁻²
		Near, Far	Near, Far
Non ^{13}CO -detects	0.05	2.5, 2.25	1.05, 1.2
	0.25	5.0, 3.75	1.46, 1.72
	0.5	8.5, 6.0	1.88, 2.2
	0.75	16.75, 10.75	2.5, 2.88
	0.95	51.1, 26.5	3.9, 4.26
	Mean	15.6, 9.1	2.1, 2.4
^{13}CO -detects	0.05	8.5, 5.75	2.4, 2.8
	0.25	31.88, 13.25	3.5, 4.1
	0.5	73.13, 28.75	4.6, 5.4
	0.75	185.13, 70.0	6.2, 7.48
	0.95	1134.4, 322.5	9.6, 13.3
	Mean	413.8, 116.3	5.2, 6.4

NOTE—The quantiles at 0.05, 0.25, 0.5, 0.75 and 0.95 for the $\mathcal{A}_{12\text{CO}}$ and N_{H_2} in their sequential data and their mean values. The H_2 column density (N_{H_2}) are calculated using the $N_{\text{H}_2} = X_{\text{CO}} W_{12\text{CO}}$, where $X_{\text{CO}} = 2 \times 10^{20} \text{ cm}^{-2} (\text{K km s}^{-1})^{-1}$. The Near represents the molecular clouds in the near range (V_{LSR} from -30 km s^{-1} to 25 km s^{-1}), the Far means the molecular clouds in the far range (V_{LSR} from -95 km s^{-1} to -30 km s^{-1}).

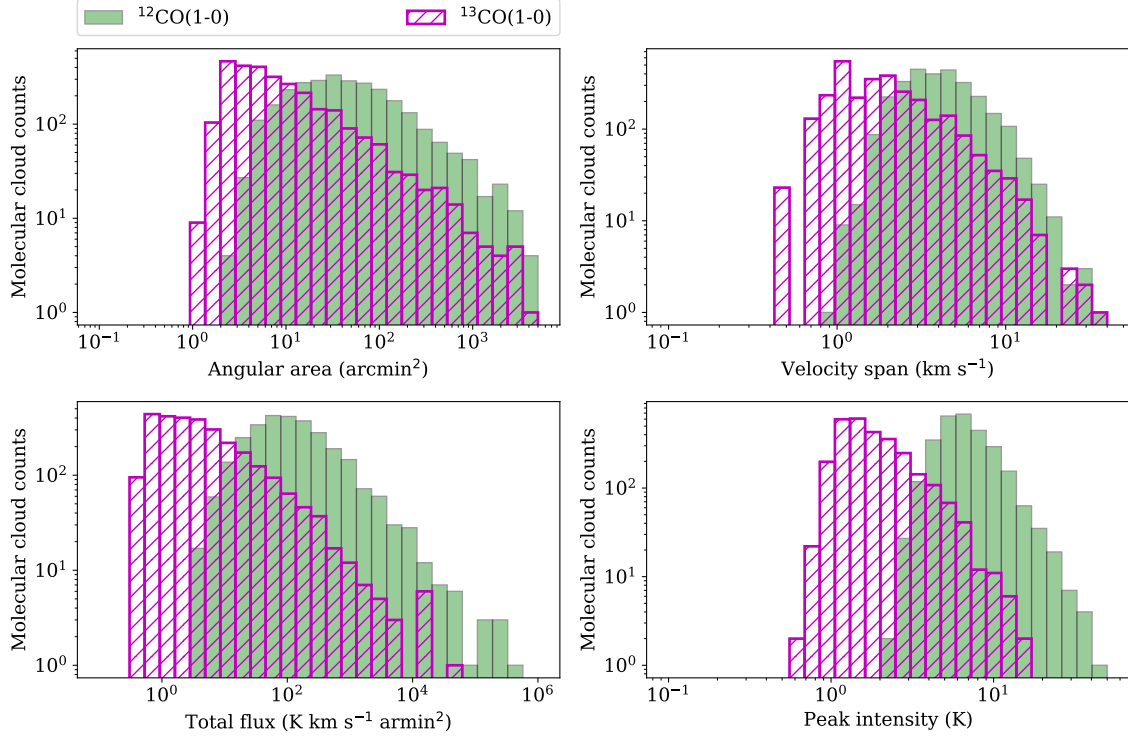


Figure 7. The number distributions of the angular sizes, velocity spans, the total fluxes and the peak intensities of $^{13}\text{CO}(1-0)$ and $^{12}\text{CO}(1-0)$ line emission for the 2,851 ^{13}CO -detects. The green histograms represent parameters of the ^{12}CO line emission. The magenta ones are the parameters of the ^{13}CO line emission.

to the spiral structure of the Milky Way, the kinematical distances, which are estimated using the Bayesian distance calculator in Reid et al. (2016), center on about ~ 0.5 kpc for molecular clouds in the Local arm and ~ 2 kpc for that in the Perseus arm. Considering these typical distances, the molecular cloud in the local region with an angular size of $1'$ has a physical scale of ~ 0.15 pc, the value is ~ 0.6 pc for that in the Perseus arm.

In addition, we estimate the averaged velocity-integrated intensities of ^{12}CO lines emission, $W_{\text{aver},^{12}\text{CO}} = \int T_{\text{mb}}(l, b, v) dv dl db / \int dl db$, for molecular clouds in the near and far groups, respectively. Their distributions are shown in Figure 6. The H_2 column density (N_{H_2}) can be calculated through the $N_{\text{H}_2} = X_{\text{CO}} W_{^{12}\text{CO}}$, where $X_{\text{CO}} = 2 \times 10^{20} \text{ cm}^{-2} (\text{K km s}^{-1})^{-1}$ is the CO-to- H_2 conversion factor (Bolatto et al. 2013). The quantile values of N_{H_2} for Non ^{13}CO -detects and ^{13}CO -detects are also listed in Table 4. We find that the typical values of $\mathcal{A}_{^{12}\text{CO}}$ and N_{H_2} of ^{13}CO -detects are larger than those of Non ^{13}CO -detects, either in the near or far groups. Thus the ^{13}CO emission seems to be related to the properties of ^{12}CO emissions independent of the distance.

Compared with the Non ^{13}CO -detects, the ^{13}CO -detects tend to have larger $\mathcal{A}_{^{12}\text{CO}}$, higher $T_{\text{peak},^{12}\text{CO}}$, and $W_{\text{aver},^{12}\text{CO}}$, either in near or far group.

4.2. ^{12}CO and ^{13}CO lines emission in ^{12}CO molecular clouds having ^{13}CO structures

To systematically analyze what properties of MCs determine the ^{13}CO line emission in the ^{13}CO -detects, we examine the correlation between their physical properties of ^{13}CO line emission with that of the ^{12}CO line emission.

4.2.1. Distribution of ^{13}CO and ^{12}CO emission parameters

Figure 7 presents the number distributions of angular sizes ($\mathcal{A}_{^{12}\text{CO}}$, $\mathcal{A}_{^{13}\text{CO}}$), velocity spans ($V_{\text{span},^{12}\text{CO}}$, $V_{\text{span},^{13}\text{CO}}$), the integrated fluxes ($F_{^{12}\text{CO}}$, $F_{^{13}\text{CO}}$), and peak intensities ($T_{\text{peak},^{12}\text{CO}}$, $T_{\text{peak},^{13}\text{CO}}$) of ^{12}CO and ^{13}CO lines emission of the 2,851 ^{13}CO -detects. The quantiles at 0.05, 0.25, 0.5, 0.75, and 0.95 of these parameters for ^{13}CO line emission are listed in Table 5. Those for ^{12}CO line emission are listed in Table 3. We find that the values of angular areas, velocity spans, peak intensities, and the integrated fluxes of ^{13}CO structures in the MCs are systematically smaller than that of their ^{12}CO line emission.

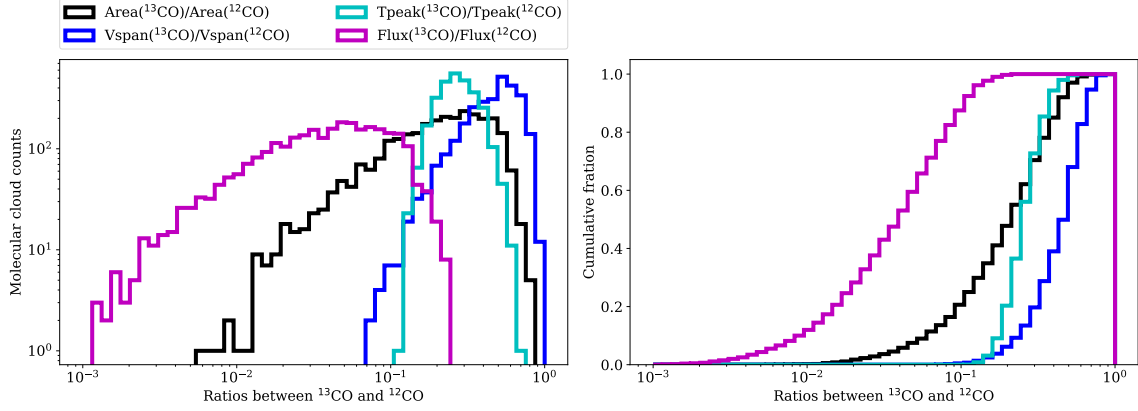


Figure 8. The counts distributions (**left panel**) and cumulative fractions (**right panel**) of the ratios between the parameters of ^{13}CO structures and that of ^{12}CO line emission for the 2,851 ^{13}CO -detects, these parameter ratios include their angular sizes (black), velocity spans (blue), the peak intensities (cyan) and the integrated fluxes (magenta).

Table 5. The physical parameters ^{13}CO emission and the ratios between the parameters of the ^{13}CO and ^{12}CO emission.

Types	Quantile	Angular area (arcmin ²)	V_{span} (km s ⁻¹)	Peak Intensity (K)	Flux (K km s ⁻¹ arcmin ²)
^{13}CO emission	0.05	2.0	0.66	1.0	0.6
	0.25	3.25	1.16	1.3	1.2
	0.5	6.25	1.66	1.6	3.1
	0.75	16.5	2.66	2.3	10.7
	0.95	120.0	6.31	4.7	121.9
	Mean	58.4	2.37	2.1	82.0
$^{13}\text{CO}/^{12}\text{CO}$	0.05	0.04	0.20	0.17	0.006
	0.25	0.12	0.36	0.22	0.02
	0.5	0.22	0.50	0.27	0.04
	0.75	0.35	0.61	0.33	0.07
	0.95	0.53	0.76	0.44	0.13
	Mean	0.25	0.48	0.28	0.05

NOTE—The quantiles at 0.05, 0.25, 0.5, 0.75 and 0.95 for each parameter in its sequential data and its mean value.

4.2.2. Ratios between ^{13}CO and ^{12}CO emission parameters

Since only a portion molecular gas components in a ^{12}CO cloud have ^{13}CO emission, what are the specific fractions of ^{13}CO gas in these ^{12}CO MCs? Figure 8 presents the distributions of the ratios between the ^{13}CO emission parameters and ^{12}CO emission parameters in the each ^{12}CO cloud with ^{13}CO structures. The quantiles at 0.05, 0.25, 0.5, 0.75, and 0.95 of these ratio values are listed in Table 5. We find that the median and mean values of $\mathcal{A}_{^{13}\text{CO}}/\mathcal{A}_{^{12}\text{CO}}$ and $T_{\text{peak},^{13}\text{CO}}/T_{\text{peak},^{12}\text{CO}}$ are close to ~ 0.25 . In addition, the 95% of the ^{13}CO -detects have the $\mathcal{A}_{^{13}\text{CO}}/\mathcal{A}_{^{12}\text{CO}}$ with values less than 0.53 and the $T_{\text{peak},^{13}\text{CO}}/T_{\text{peak},^{12}\text{CO}}$ with values less than 0.44. For the $V_{\text{span},^{13}\text{CO}}/V_{\text{span},^{12}\text{CO}}$ in the ^{13}CO -detects, their median and mean values are about 0.5 and 95% of them are less than 0.76. The median and mean values of $F_{^{13}\text{CO}}/F_{^{12}\text{CO}}$, are 0.04 and 0.05, respectively. Moreover, the $F_{^{13}\text{CO}}/F_{^{12}\text{CO}}$ for the 95% of ^{13}CO -detects is not larger than 0.13. That implies the fractions of ^{13}CO gas in the ^{12}CO molecular clouds are typically less than 13%. Considering the ^{12}CO lines are more optically thick, this value should be much lower.

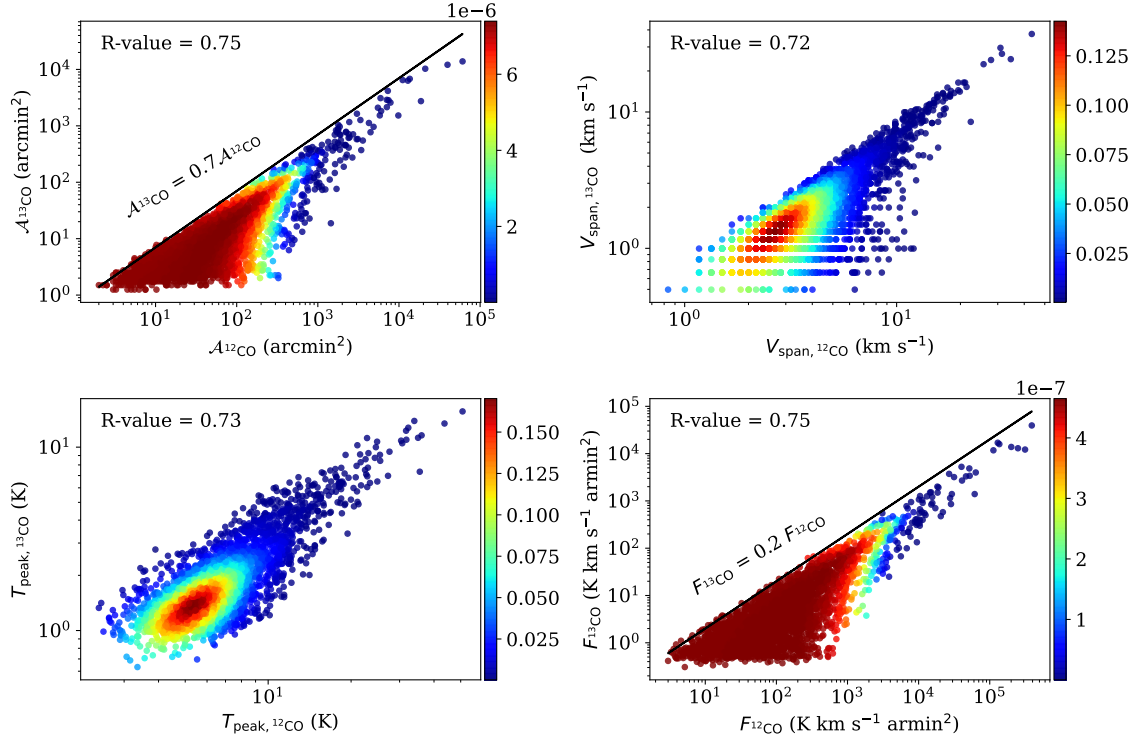


Figure 9. The correlations of angular sizes, velocity spans, peak intensities, and integrated fluxes of $^{12}\text{CO}(1-0)$ emission between that of $^{13}\text{CO}(1-0)$ line emission. Each dot represents a ^{12}CO cloud with ^{13}CO structures. The ^{12}CO emission parameters of a ^{12}CO cloud represent the global physical parameters of a ^{12}CO clouds. The ^{13}CO emission parameters are derived from all the ^{13}CO structures inside a single ^{12}CO cloud. The black lines represent the upper limits ($\mathcal{A}_{13\text{CO}}$ vs $\mathcal{A}_{12\text{CO}}$, $F_{13\text{CO}}$ vs $F_{12\text{CO}}$). The colors on the points represent the distribution of the probability density function of the ^{13}CO -detects counts (2D-PDF), which are calculated utilizing the Kernel-density estimation through Gaussian kernels in the PYTHON package [scipy.stats.gaussian_kde](https://docs.scipy.org/doc/scipy/stats/gaussian_kde.html).

4.2.3. Correlation between ^{13}CO and ^{12}CO emission parameters

Since the parameters of ^{13}CO line emission are distributed in a certain range, how do the global properties of molecular clouds affect their ^{13}CO line emission? Figure 9 presents the correlations between the parameters of ^{13}CO emission and that of ^{12}CO emission in each ^{13}CO -detects. The spearman's rank correlation coefficients (R-value) for these relations are estimated and the resultant R-values are noted in the Figure 9. We find the R-value (0.75) for $\mathcal{A}_{12\text{CO}}$ and $\mathcal{A}_{13\text{CO}}$ is consistent with that for $F_{13\text{CO}}$ and $F_{12\text{CO}}$, a little higher than the R-value (0.73) for $T_{\text{peak},13\text{CO}}$ and $T_{\text{peak},12\text{CO}}$ and the value of 0.72 for the $V_{\text{span},12\text{CO}}$ and $V_{\text{span},13\text{CO}}$. That implies there are roughly positive correlations between them, but they still present a little dispersed.

There are sharp upper limits for the ratios of $\mathcal{A}_{13\text{CO}}/\mathcal{A}_{12\text{CO}}$, and $F_{13\text{CO}}/F_{12\text{CO}}$ independent of the angular areas and CO integrated fluxes in wide ranges. As shown in Figure 9, we outline their upper limits with slopes of 0.7 and 0.2, respectively. That indicates the area of ^{13}CO emission in a molecular cloud generally does not exceed the 70% of the ^{12}CO emission area, independent of the ^{12}CO emission area. For the integrated fluxes, the ^{13}CO emission fluxes are usually less than 20% of the ^{12}CO emission fluxes.

Overall, the global physical parameters of molecular clouds, such as the angular areas and integrated fluxes of ^{12}CO emission, show roughly positive correlations and provide upper limits for that of ^{13}CO emission. Whereas they cannot critically determine the ^{13}CO emission.

Since the correlation between the global physical properties of each ^{12}CO cloud and that of its interior ^{13}CO structures exhibits a bit scattered, we further focus on the local areas having both ^{12}CO and ^{13}CO line emissions in each ^{12}CO cloud with ^{13}CO structures. Figure 10 presents the correlations between the parameters of ^{12}CO and ^{13}CO emission towards the same areas where both the ^{12}CO and ^{13}CO emissions are detected in each ^{13}CO -detects. The $T_{\text{aver},12\text{CO}}$ is calculated by averaging the ^{12}CO line intensities within the ^{13}CO emission region. The $T_{\text{aver},13\text{CO}}$

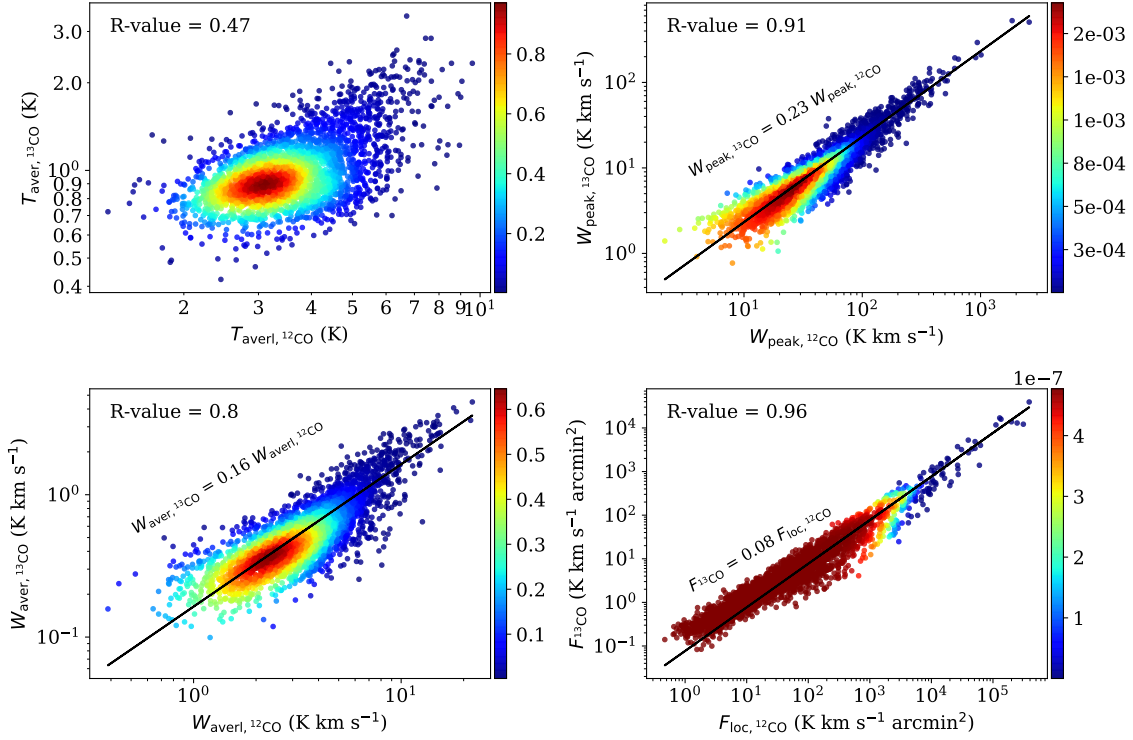


Figure 10. The correlations between the averaged line intensities ($T_{\text{aver},12\text{CO}}$ vs $T_{\text{aver},13\text{CO}}$), peak ($W_{\text{peak},12\text{CO}}$ vs $W_{\text{peak},13\text{CO}}$) and averaged ($W_{\text{aver},12\text{CO}}$ vs $W_{\text{aver},13\text{CO}}$) velocity-integrated intensities, and the integrated fluxes ($F_{\text{loc},12\text{CO}}$ vs $F_{13\text{CO}}$) of ^{12}CO and ^{13}CO emission towards the same areas where both the ^{12}CO and ^{13}CO emissions are detected in each ^{13}CO -detects. Each dot represents a single ^{12}CO cloud with ^{13}CO structures. The parameters of ^{12}CO line emission are the physical parameters toward the ^{13}CO -emitting regions within ^{12}CO clouds. The ^{13}CO emission parameters are derived from all the ^{13}CO structures inside a single ^{12}CO cloud. The black lines show the linear least-squares fits to the data. The colors on the points show the distribution of the probability density function of the ^{13}CO -detects counts (2D-PDF).

is the mean value of the ^{13}CO spectra intensities. The $W_{\text{aver},13\text{CO}}$ and $W_{\text{aver},12\text{CO}}$ are the averaged values of the velocity-integrated intensities of ^{13}CO line and that of ^{12}CO line in the ^{13}CO emission region, respectively. The $W_{\text{peak},13\text{CO}}$ and $W_{\text{peak},12\text{CO}}$ are the peak values of the velocity-integrated intensity of ^{13}CO lines and that of ^{12}CO lines at the same positions, respectively. The $F_{13\text{CO}}$ and $F_{\text{loc},12\text{CO}}$ represent the integrated fluxes of ^{13}CO line emission and that of ^{12}CO emission in the ^{13}CO emission area, respectively. We calculate their spearman's rank correlation coefficients (R-value) and the resultant R-values are noted in Figure 10. Based on these relations between $W_{\text{aver},13\text{CO}}$ and $W_{\text{aver},12\text{CO}}$ (R-value = 0.8), $W_{\text{peak},13\text{CO}}$ and $W_{\text{peak},12\text{CO}}$ (R-value = 0.91), and $F_{13\text{CO}}$ and $F_{\text{loc},12\text{CO}}$ (R-value = 0.96), their correlations are more and more tightly. That indicates the properties of ^{12}CO line emission in the area where both ^{12}CO and ^{13}CO are detected, its velocity-integrated intensity ($W_{12\text{CO}}$) in this area, is a more direct link for that of ^{13}CO line emission.

Furthermore, we also implement the linear least-squares to these linear relations and the fitted slopes are noted in Figure 10. These relations indicate that the ^{13}CO fluxes linearly increase as the ^{12}CO fluxes increases in the region, where the $W_{12\text{CO}}$ is larger than a value of $\sim 1 \text{ K km s}^{-1}$, which is close to the sensitivities of MWISP data.

4.2.4. The counts of ^{13}CO molecular structures in a single ^{12}CO molecular cloud

The boundary of a molecular cloud is defined by its $^{12}\text{CO}(1-0)$ line emission, its internal ^{13}CO molecular structures can present several individual structures, as shown in Figure C10. The counts of ^{13}CO molecular structures in a single ^{12}CO cloud can provide essential clues to the development of dense gas content and the internal sub-structures of molecular clouds. We statistic the number of separate ^{13}CO molecular structures in each ^{13}CO -detects. Owing to that the molecular cloud distance may affect the spatial physical resolution of ^{13}CO molecular structures, we divide the 2,851 ^{13}CO -detects into the near and far groups, as introduced in Section 4.1. Figure 11 presents the distributions

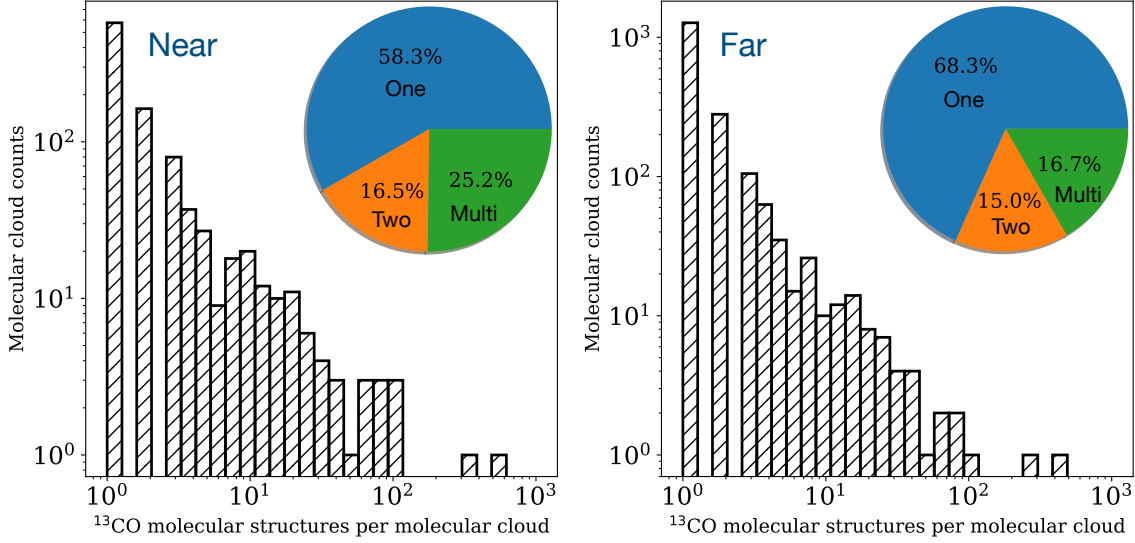


Figure 11. The distribution of the ^{13}CO structure counts in a single ^{12}CO cloud for the ^{13}CO -detects in the near (left panel) and far (right panel) groups, respectively. In the right-up corner of each panel, the pie chart illustrates the percentages of ^{12}CO clouds in this sample with one ^{13}CO structure, two ^{13}CO structures, and multiple (more than two) ^{13}CO structures, respectively.

Table 6. The number detection rates and the total flux ratios in the total molecular clouds, nonfilaments, and filaments.

Types	All	Nonfilament	filament
Number detection rate	15.7%	14.0%	56.5%
Flux ratio	6.3%	2.9%	6.7%

NOTE—The number detection rate is the number of extracted ^{13}CO -detects divided by the number of molecular clouds in the total samples, nonfilaments and filaments, respectively. The flux ratio is the total integrated fluxes of ^{13}CO line emission divided by that of ^{12}CO line emission for the total molecular clouds, nonfilaments and filaments, respectively.

of ^{13}CO molecular structure counts in a single ^{12}CO cloud for the ^{13}CO -detects in near and far groups, respectively. We find that the ^{13}CO -detects with one ^{13}CO structure are dominant and take a percentage of about 60%. Then the molecular clouds having two ^{13}CO molecular structures occupied about 15% of the ^{13}CO -detects. The rest $\sim 20\%$ of ^{13}CO -detects have more than two ^{13}CO structures, the ^{13}CO structure counts in a single ^{12}CO cloud can be up to ~ 600 . It should be noted that the number fraction of ^{12}CO clouds with one ^{13}CO velocity structure varies about 10% for that in the near and far groups, as well as the fraction of ^{12}CO clouds with multiple ^{13}CO structures.

4.3. Linking the internal ^{13}CO gas structures to the morphologies of ^{12}CO clouds

4.3.1. The ^{13}CO structures detection rates and morphologies

In paper I (Yuan et al. 2021), we took the morphological classification for the total 18,190 molecular clouds, which were classified as unresolved, non-filaments (11,680), and filaments (2,062). Among the 2,851 ^{13}CO -detects, 1,641 ^{12}CO molecular clouds belong to nonfilaments and 1,166 clouds are classified as filaments. We find that the number

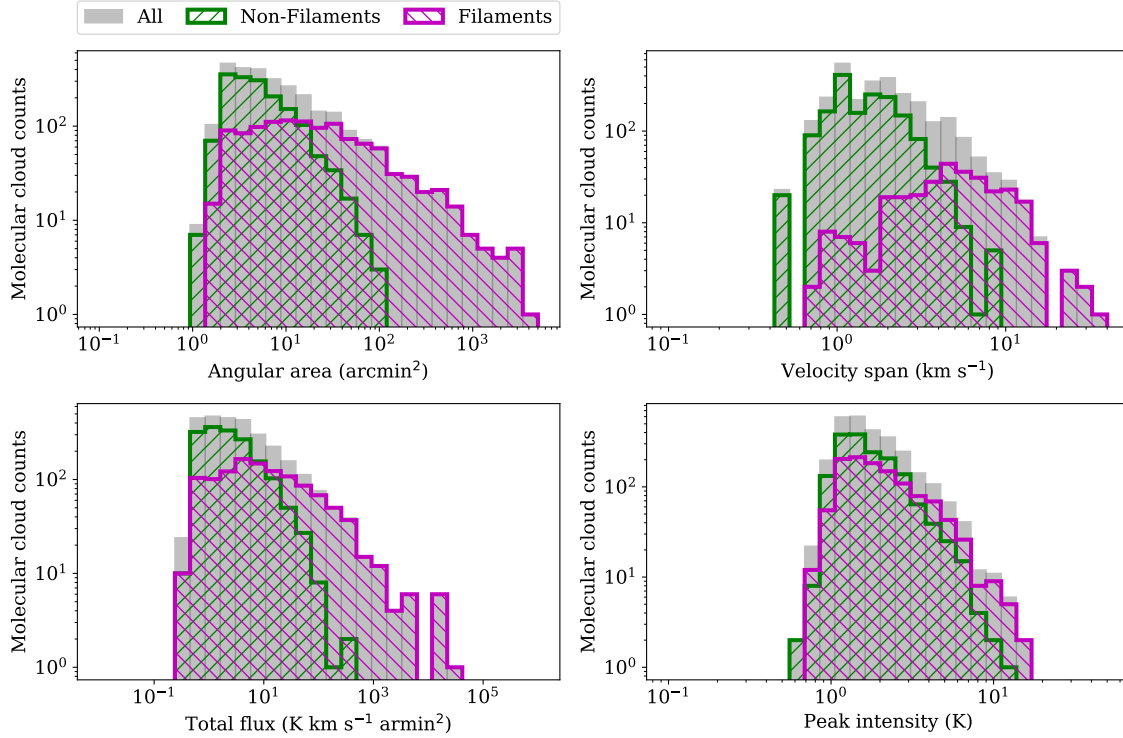


Figure 12. The number distributions of angular sizes, velocity spans, the total fluxes and the peak intensities of $^{13}\text{CO}(1-0)$ line emission for the ^{13}CO -detects classified as filaments and nonfilaments.

detection rate of ^{13}CO structures is 15.7%(2851/18190) in the whole ^{12}CO molecular clouds, 14% (1641/11680) in the ^{12}CO clouds classified as nonfilaments, and 56.5% (1166/2062) in the ^{12}CO clouds classified as filaments. For the ratio of the total integrated fluxes of ^{13}CO line emission to that of ^{12}CO line emission, the value is 6.3% for the total molecular clouds, 2.9% for the nonfilaments, and 6.7% for the filaments. Those values are listed in Table 6. Thus, compared with nonfilaments, the filaments tend to have higher density gas structures, which are traced by ^{13}CO lines.

4.3.2. The ^{13}CO structures parameters and morphologies

Furthermore, we focus on the properties of the ^{13}CO molecular gas structures in the filaments and nonfilaments of the 2,851 ^{13}CO -detects. Figure 12 compares the ^{13}CO structures parameters of these filaments and nonfilaments. We find that the angular areas ($\mathcal{A}_{^{13}\text{CO}}$), velocity spans ($V_{\text{span},^{13}\text{CO}}$) and integrated fluxes ($F_{^{13}\text{CO}}$) of ^{13}CO structures in these filaments tend to be larger than that in these nonfilaments. While the number distributions of their peak intensities are similar. We find that filaments not only tend to have ^{13}CO gas structures, but also their internal ^{13}CO structures have larger angular sizes, velocity span, and integrated fluxes. That indicates the ^{12}CO cloud classified as filaments gather more high-density gas structures in the local areas where both ^{12}CO and ^{13}CO emissions are detected.

We also link the ^{13}CO molecular structure counts in a single ^{12}CO cloud to its morphology. Figure 13 illustrates the distribution of ^{13}CO molecular structure counts within one ^{12}CO cloud for the ^{13}CO -detects classified as filaments and nonfilaments. We find that about 85% of these nonfilaments have one ^{13}CO molecular structure and only 3% of nonfilaments have more than two ^{13}CO molecular structures. While for these filaments, those with one ^{13}CO molecular structure only occupy about 35%, and those having more than two ^{13}CO molecular structures take about 44%. Moreover, only filaments could harbor more than ten ^{13}CO structures. That indicates the filament tend to have more separate ^{13}CO molecular structures in its interior. That implies the development of dense gas content in filaments is separate and inhomogenous.

5. DISCUSSION

5.1. Comparison with previous works

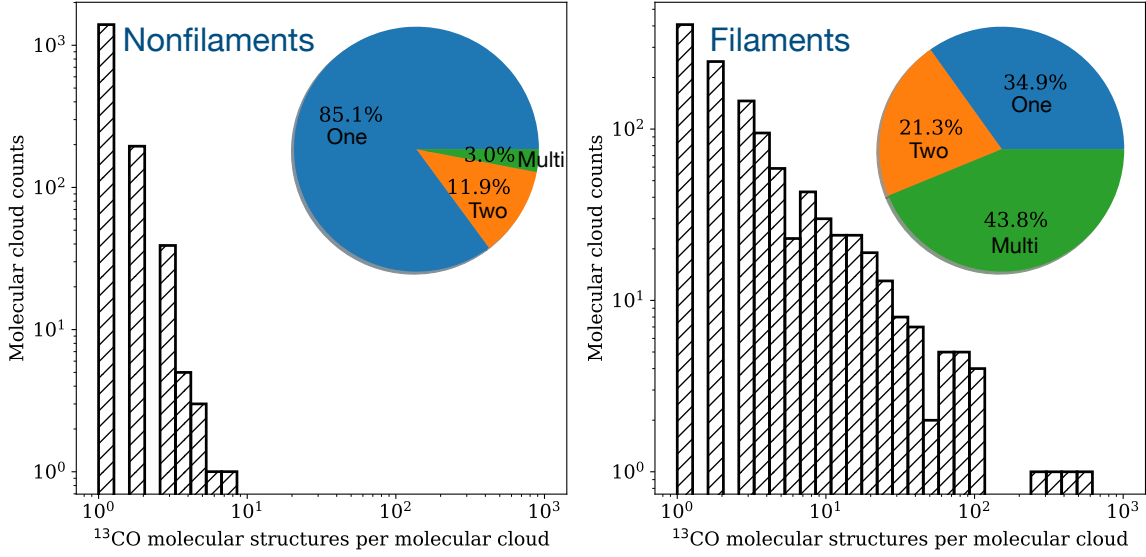


Figure 13. The distribution of the ^{13}CO molecular structure counts in a single ^{12}CO cloud for the ^{13}CO -detects classified as nonfilaments (left panel) and filaments (right panel) groups, respectively. In the right-up corner of each panel, the pie chart illustrates the percentages of MCs in this sample with one ^{13}CO molecular structure, two ^{13}CO molecular structures, multiple (larger than two) ^{13}CO molecular structures, respectively.

In the Milky Way, [Torii et al. \(2019\)](#) used the CO $J = 1 - 0$ data from the FUGIN project and found that the ratio of the integrated intensities of ^{13}CO and ^{12}CO lines ($W(^{13}\text{CO})/W(^{12}\text{CO})$) along the Galactical longitude $l = 10^\circ - 50^\circ$ were distributed in a range of 1% – 10%. While the $W(^{13}\text{CO})/W(^{12}\text{CO})$ in the star-forming cloud Orion B can achieve about 15% ([Gratier et al. 2021](#)). [Roman-Duval et al. \(2016\)](#) investigated the Galactic distribution of molecular gas components traced by ^{12}CO and ^{13}CO lines along the Galactic radius. The values of $W(^{13}\text{CO})/W(^{12}\text{CO})$ have an approximately constant value of 20% out to the galactic radius of 6.5 kpc, decrease to $\sim 8\% - 10\%$ in the solar neighborhood and about 5% – 10% out to the radius of 14 kpc.

In the nearby galaxies, [Cormier et al. \(2018\)](#) carried out the CO observations for nine nearby spiral galaxies using IRAM 30-m telescope, which has a spatial resolution of ~ 1.5 kpc, the resultant $W(^{13}\text{CO})/W(^{12}\text{CO})$ ratio has a median value of $\sim 9\%$ and varies by a factor of 2. For the five nearby star-forming galaxies, [Gallagher et al. \(2018\)](#) combined the IRAM $^{12}\text{CO}(1-0)$ maps and ALMA observations of $^{13}\text{CO}(1-0)$ lines and presented the distribution of the $W(^{13}\text{CO})/W(^{12}\text{CO})$ along the radius, which have a mean value of 8.8% with a radius less than 1 kpc and 3.9% in a radius larger than 1 kpc. Furthermore, [Méndez-Hernández et al. \(2020\)](#) presented the ALMA observations towards 27 low-redshift ($0.02 < z < 0.2$) star-forming galaxies, their averaged value of $W(^{13}\text{CO})/W(^{12}\text{CO})$ is $5.6 \pm 1\%$ and varies by a factor of 2.

Figure 14 compares the above literature results with our results. Overall, the $W(^{13}\text{CO})/W(^{12}\text{CO})$ depends on not only the molecular cloud conditions but also their positions in the galaxy. Moreover, the $W(^{13}\text{CO})/W(^{12}\text{CO})$ in the local molecular clouds with active star formation rates is higher.

5.2. Implications of molecular clouds formation and evolution

The questions of how molecular clouds form and what mechanisms determine their physical properties still remain open. Several mechanisms have been invoked to explain the gathering mass of molecular clouds. The agglomeration of smaller clouds ([Oort 1954](#); [Field & Saslaw 1965](#); [Kwan & Valdes 1983](#); [Tomisaka 1984](#)), the turbulence flows in the diffuse ISM ([Vazquez-Semadeni et al. 1995](#); [Passot et al. 1995](#); [Ballesteros-Paredes et al. 1999a](#)), and the large-scale gravitational instability of the Galactic disk ([Lin & Shu 1964](#); [Roberts 1969](#); [Tasker & Tan 2009](#)).

From our observations of 18,190 molecular clouds using ^{12}CO and ^{13}CO lines. In terms of their morphologies, i.e., nonfilaments and filaments, filaments tend to have larger spatial scales. Whereas their averaged H_2 column densities do not vary significantly ([Yuan et al. 2021](#)). Furthermore, we find that ^{13}CO gas emission determined by the its H_2

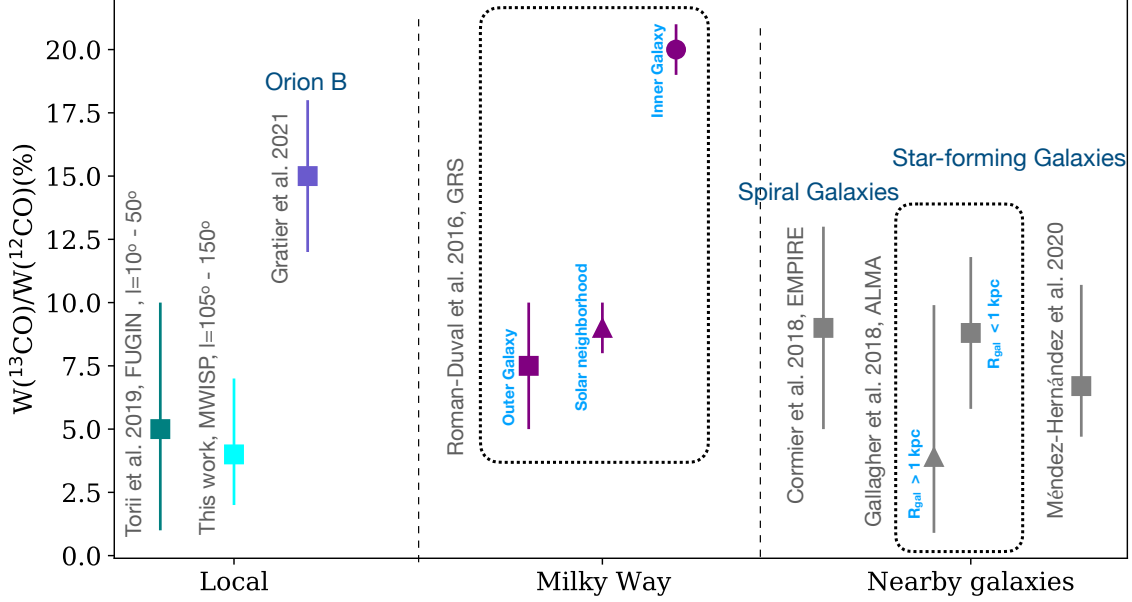


Figure 14. Comparisons among the integrated intensity ratios between ^{13}CO and ^{12}CO lines ($W(^{13}\text{CO})/W(^{12}\text{CO})$). The colored points show the average or median values of $W(^{13}\text{CO})/W(^{12}\text{CO})$. The error bars on the individual points reflect the distributions for the ratios. From left to right, we present the literature results of $W(^{13}\text{CO})/W(^{12}\text{CO})$ in the local regions of Milky Way and in the nearby galaxies, respectively. The $W(^{13}\text{CO})/W(^{12}\text{CO})$, which is presented in Figure 12 of Torii et al. (2019), is calculated through the total velocity-integrated intensities of ^{13}CO emission in a Galactic longitude of 1 degree divided by that of ^{12}CO emission in the same bin. The presented values of this work is the ratio of the total integrated intensities of ^{13}CO emission to that of ^{12}CO emission in each molecular cloud. The $W(^{13}\text{CO})/W(^{12}\text{CO})$ for the Orion B is the mean integrated intensity of ^{13}CO emission divided by that of ^{12}CO emission, whose values are listed in Table 2 of Gratier et al. (2021). The values of $W(^{13}\text{CO})$ and $W(^{12}\text{CO})$ in Roman-Duval et al. (2016); Cormier et al. (2018); Gallagher et al. (2018); Méndez-Hernández et al. (2020) are corresponds to their total luminosities in a Galactocentric radius bin, divided by the surface areas covered by the surveys in that bin, further projected onto the Galactic disk.

column density is primarily detected in the filaments. That indicates the filament gathers more mass on a global scale and meanwhile has local density enhancements where both ^{12}CO and ^{13}CO emissions are detected. In addition, the filament also tends to have more than one individual structure traced by ^{13}CO lines in its interior. That implies the development of dense gas content in filaments is separate and inhomogenous. The formation of filament often arises from the shock compression in the ISM (Arzoumanian et al. 2018; Abe et al. 2021; Arzoumanian et al. 2022). The shock compression may be caused by supersonic turbulence in the molecular clouds (Padoan & Nordlund 1999; Pudritz & Kevlahan 2013; Matsumoto et al. 2015), cloud collisions (Inoue & Fukui 2013; Inoue et al. 2018; Tokuda et al. 2019), feedback from massive stars, and galactic spiral shock. While the supercritical filaments may be driven by the gravitational contraction/accretion (Arzoumanian et al. 2013; Gong et al. 2021; Yuan et al. 2020) and further fragment into smaller components owing to turbulence and gravitational instabilities (Hacar & Tafalla 2011; Henshaw et al. 2016; Kainulainen et al. 2017; Lu et al. 2018; Lin et al. 2019; Yuan et al. 2019).

We try to investigate the relation between the filaments and nonfilaments. If the filaments fragment into nonfilaments due to the gravitational instability, the high-density gas fraction in nonfilaments should be comparable to that of filaments. That is unlikely owing to our observational results of nonfilaments with less dense gas. Our observed properties of filaments and nonfilaments favor that molecular clouds be explained as the density fluctuations induced by the turbulent compression in the diffuse ISM and broken up by the combination of dynamical and thermal instabilities, like the physical processes of shear, rotation, cooling, and magnetic fields (Ballesteros-Paredes et al. 1999b; Koyama & Inutsuka 2002; Heitsch et al. 2006; Vázquez-Semadeni et al. 2006; Beuther et al. 2020). Filaments tend to be under shock compressions and nonfilaments tend to be in low-pressure environments. Meanwhile they present the different spatial scales and internal structures. In addition, we are not able to rule out the hypothesis that nonfilament collisions to form filaments to some degree.

6. SUMMARY AND CONCLUSIONS

We identify the ^{13}CO gas structures in the 18,190 ^{12}CO molecular clouds and systematically compare the physical properties of ^{12}CO clouds having ^{13}CO gas structures (^{13}CO -detects) and those of ^{12}CO clouds without ^{13}CO gas structures (Non ^{13}CO -detects). Furthermore, we systematically analyze the ^{13}CO and ^{12}CO emission parameters in the 2851 ^{13}CO -detects, and link the internal ^{13}CO gas structures of each ^{12}CO cloud with its morphology, i.e., filament or nonfilament. The main conclusions are as follows:

1. In the whole sample of 18,190 ^{12}CO molecular clouds, $\sim 15.7\%$ ^{12}CO clouds (2851) have the ^{13}CO molecular gas structures. The total integrated fluxes of ^{12}CO line emission for the ^{13}CO -detects are about 93% of that for the whole sample of molecular clouds.
2. In the 2851 ^{13}CO -detects, we find the ^{13}CO structures' area in a ^{12}CO cloud generally does not exceed 70% of the ^{12}CO emission area, independently of the ^{12}CO emission area, and its interior integrated fluxes of ^{13}CO emission are usually less than 20% of those of its ^{12}CO emission.
3. In the 2851 ^{13}CO -detects, we find a strong correlation between the velocity-integrated intensities of ^{12}CO lines and those of ^{13}CO lines emission in the same areas where both the ^{12}CO and ^{13}CO emissions are detected.
4. In the 2851 ^{13}CO -detects, we find that there are $\sim 60\%$ of ^{12}CO clouds have one individual ^{13}CO structure, about 15% of ^{12}CO clouds have two separate ^{13}CO structures, and the rest of them have more than two separate ^{13}CO structures.
5. We link the ^{13}CO gas fractions in the ^{13}CO -detects with their morphologies, i.e., filaments or nonfilaments, and find that the ^{13}CO line emissions are primarily detected in the ^{12}CO clouds classified as filaments. In addition, a filament tends to have more than one individual ^{13}CO structure in its interior.

We gratefully thank the anonymous referee for the constructive comments that helped improve the quality of this paper. This research made use of the data from the Milky Way Imaging Scroll Painting (MWISP) project, which is a multi-line survey in $^{12}\text{CO}/^{13}\text{CO}/\text{C}^{18}\text{O}$ along the northern galactic plane with PMO-13.7m telescope. We are grateful to all of the members of the MWISP working group, particularly to the staff members at the PMO-13.7m telescope, for their long-term support. This work was supported by the National Natural Science Foundation of China through grant 12041305. MWISP was sponsored by the National Key R&D Program of China with grant 2017YFA0402701 and the CAS Key Research Program of Frontier Sciences with grant QYZDJ-SSW-SLH047.

Software: Astropy ([Astropy Collaboration et al. 2013, 2018](#)), Matplotlib ([Hunter 2007](#))

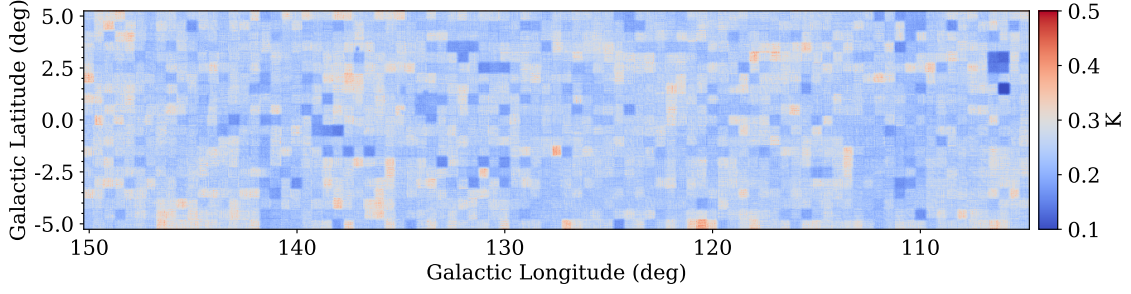


Figure A1. The distribution of the background noise RMS in the second Galactic quadrant with $104.75^\circ < l < 150.25^\circ$ and $|b| < 5.25^\circ$.

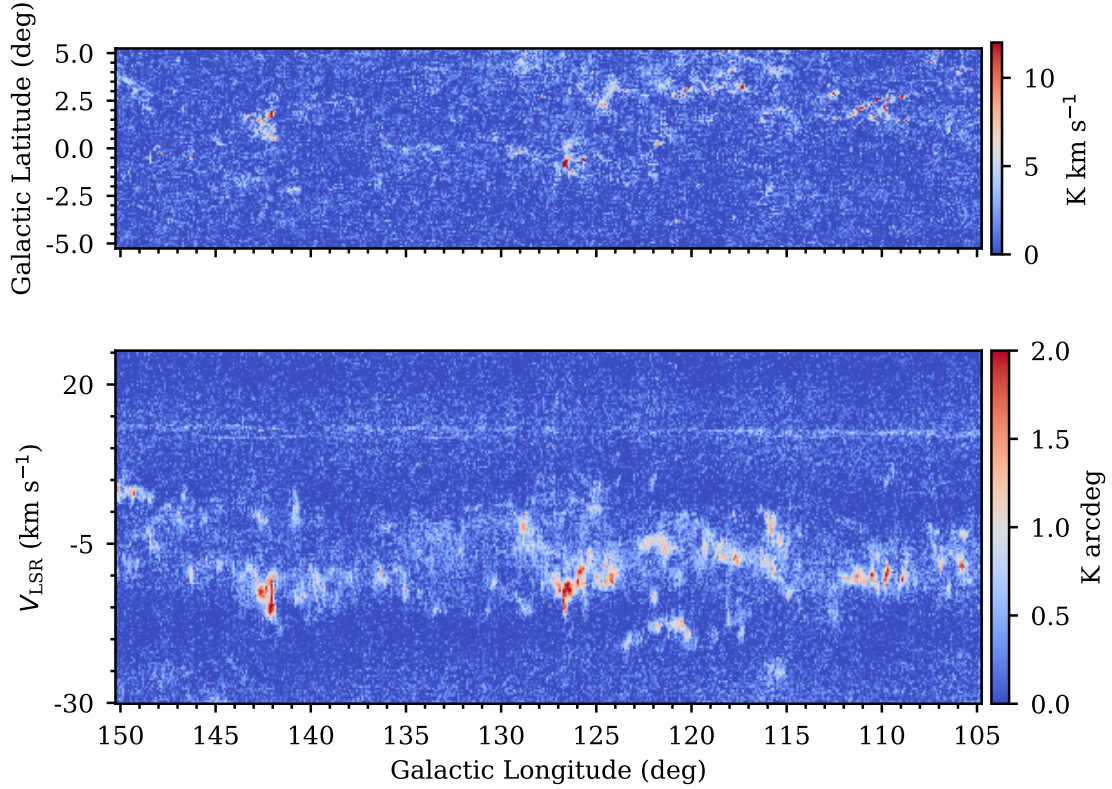


Figure A2. Top Panel: the velocity-integrated intensity map of $^{13}\text{CO}(1-0)$ emission in the near group. This map is derived by integrating the ^{13}CO emission over the velocity range between -30 km s^{-1} and 25 km s^{-1} . The sensitivity for this velocity-integrated is about 0.77 K km s^{-1} . Bottom Panel: the latitude-integrated intensity map of $^{13}\text{CO}(1-0)$ emission in the near group. This map is derived by integrating the ^{13}CO emission over the latitude range from -5.25° to 5.25° .

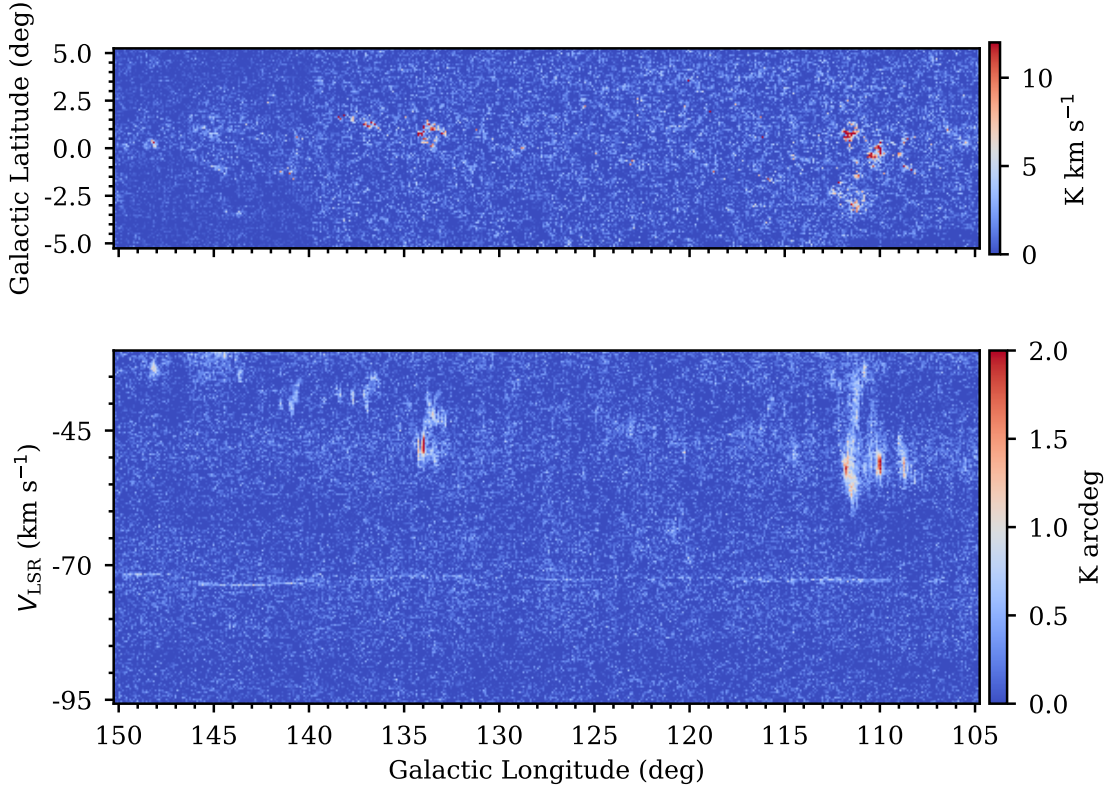


Figure A3. Top Panel: the velocity-integrated intensity map of $^{13}\text{CO}(1-0)$ emission in the far group. This map is derived by integrating the ^{13}CO emission over the velocity range between -95 km s^{-1} and -30 km s^{-1} . The sensitivity for this velocity-integrated is about 0.83 K km s^{-1} . Bottom Panel: the latitude-integrated intensity map of $^{13}\text{CO}(1-0)$ emission in the far group. This map is derived by integrating the ^{13}CO emission over the latitude range from -5.25° to 5.25° .

A. $^{13}\text{CO}(J = 1-0)$ LINES DATA

B. THE PARAMETERS OF DBSCAN ALGORITHM

The DBSCAN algorithm extracts the consecutive structures in the PPV space of CO lines data, based on a line intensity threshold and two parameters, i.e. ϵ and MinPts. Two parameters of ϵ and MinPts define the connectivity of structures in the PPV space. Each point within the extracted consecutive structure is called a core point. For a core point, its adjacent points contained in its neighborhood has to exceed a threshold. The parameter of MinPts determines the threshold of the number of adjacent points and the ϵ represents the radius of the neighborhood. A border point in the consecutive structure is defined as a point inside the ϵ -neighborhood of a core point, but not necessarily contain the MinPts neighbors, as shown in Figure 2 of (Ester et al. 1996). In the PPV space of CO data, Yan et al. (2020) has examined all the choices of parameters and ^{12}CO line intensities cutoffs to identify molecular clouds. The parameters of cutoff = 2σ , minPts = 4, $\epsilon = 1$ are used in the DBSCAN algorithm to extract the ^{12}CO molecular clouds in the ^{12}CO data cube, as well as the ^{13}CO molecular structures within the ^{12}CO molecular cloud. The post-selection criteria are examined and utilized to avoid the noise contamination (Yan et al. 2020). These criteria for a extracted structure include: (1) the minimum voxel number is 16; (2) the peak intensity is larger than the value of cutoff + 3σ for ^{12}CO or cutoff + 2σ for ^{13}CO ; (3) the angular area is large than one beam size (2×2 pixels); (4) the number of velocity channels are larger than 3.

C. THE ^{13}CO STRUCTURES OF THE MOLECULAR CLOUD G139.73 EXTRACTED BY THREE METHODS

D. RANDOM EXAMPLES OF MOLECULAR CLOUDS WITH ^{13}CO STRUCTURES

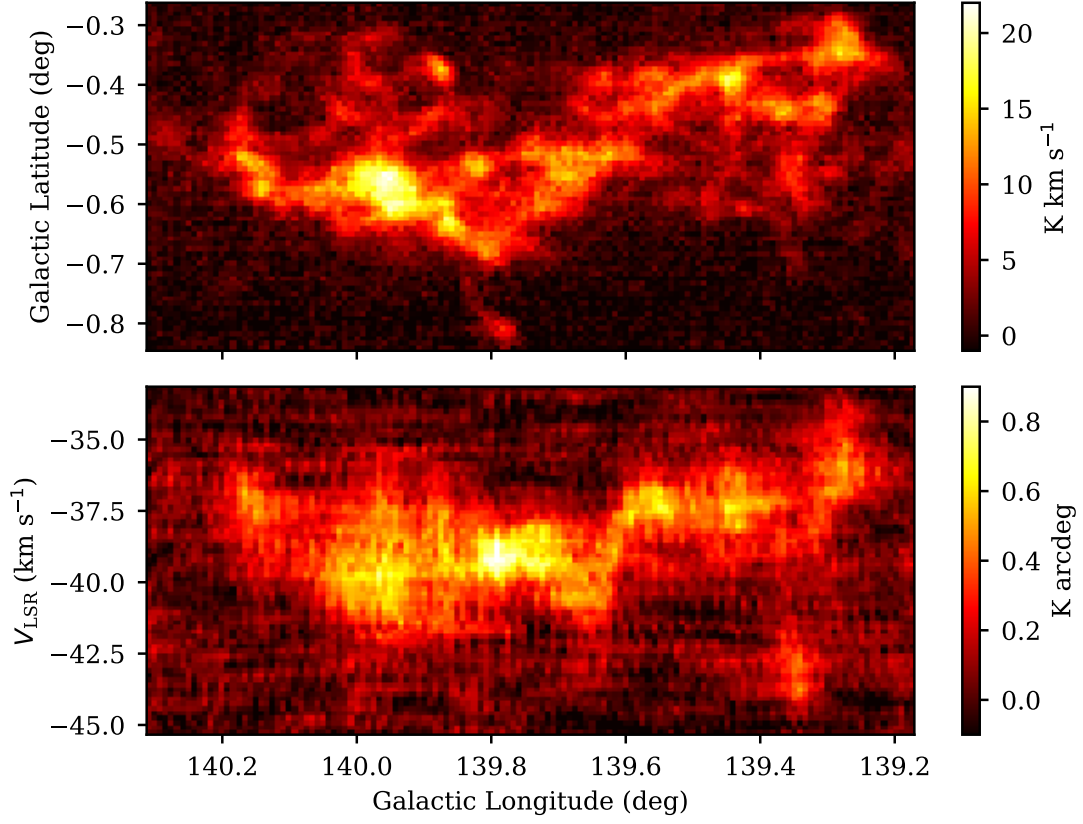


Figure C4. The velocity-integrated intensity map (**upper**) and latitude-integrated intensity map (**lower**) of ^{12}CO emission for the molecular cloud G139.73, which are derived by the raw chopped ^{12}CO data cube without any clipping.

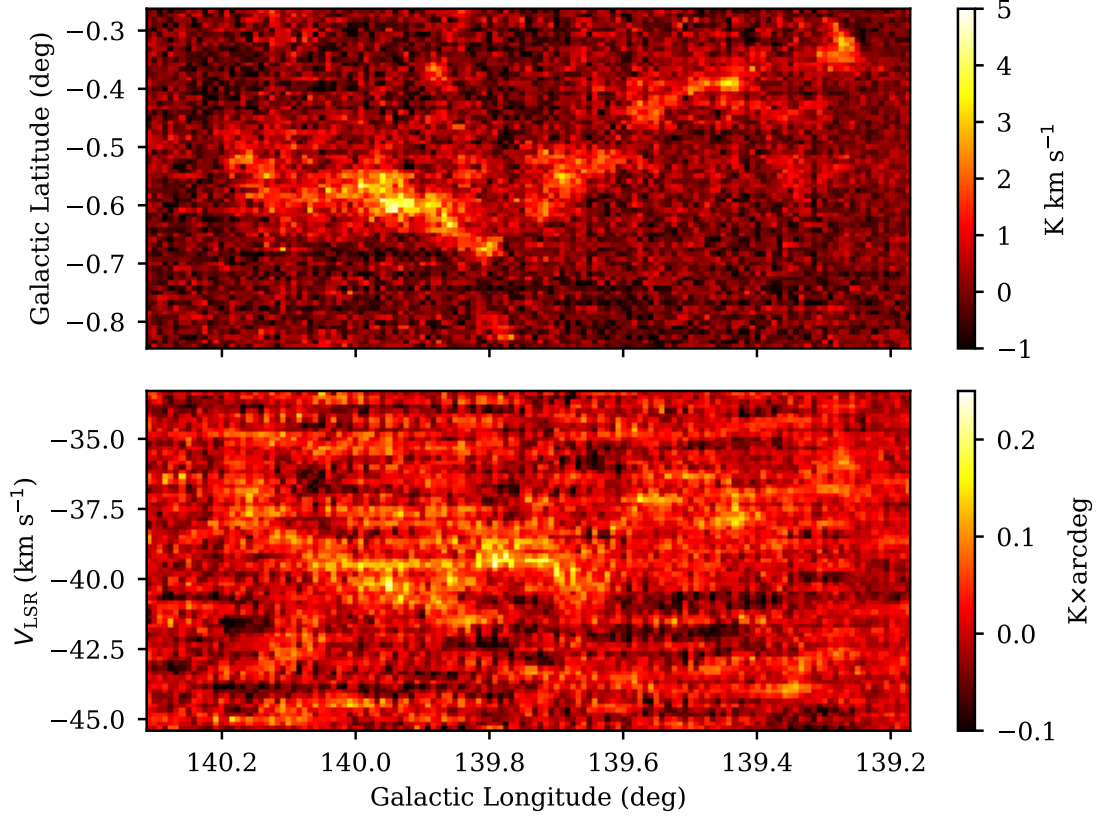


Figure C5. The velocity-integrated intensity map (**upper**) and latitude-integrated intensity map (**lower**) of ^{13}CO emission for the molecular cloud G139.73, which are derived by the raw chopped ^{13}CO data cube without any clipping.

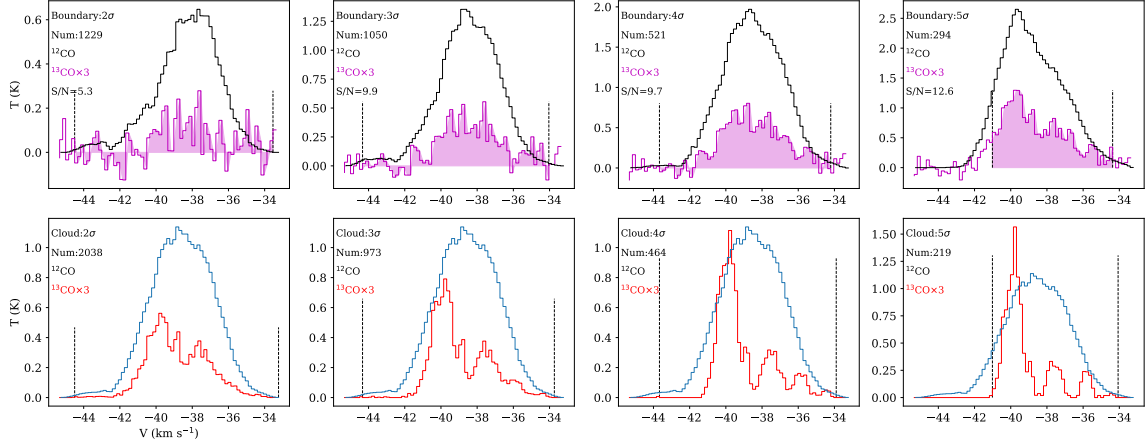


Figure C6. **Upper panels:** the mean spectrum of ^{12}CO (black) and ^{13}CO (magenta) spectral lines along the boundaries of ^{13}CO structures extracted in the molecular cloud G139.73 by the clipping at the cutoff level of 2σ , 3σ , 4σ , and 5σ , respectively. The ^{13}CO spectral lines are from the raw chopped ^{13}CO data cube without any clipping, as shown in Figure C5. The ^{12}CO spectral lines are from the extracted ^{12}CO cloud of G139.73. The noted Num in each panel is the number of the spectrum along the corresponding boundary. The S/N is the ratio of the peak intensity to the noise RMS for the averaged-boundary ^{13}CO spectrum. **Lower panels:** the mean spectrum of the extracted ^{12}CO cloud (blue) in Yan et al. (2021) and the mean spectrum of the ^{13}CO structures (red) extracted by the clipping at the cutoff level of 2σ , 3σ , 4σ , and 5σ . The vertical dashed lines illustrate the velocity span for the extracted ^{13}CO structures within G139.73 by the clipping at the corresponding cutoff levels of 2σ , 3σ , 4σ , and 5σ , respectively. All the ^{13}CO spectra are multiplied by a factor of 3. The σ value is estimated from the raw data and equal to 0.27 K

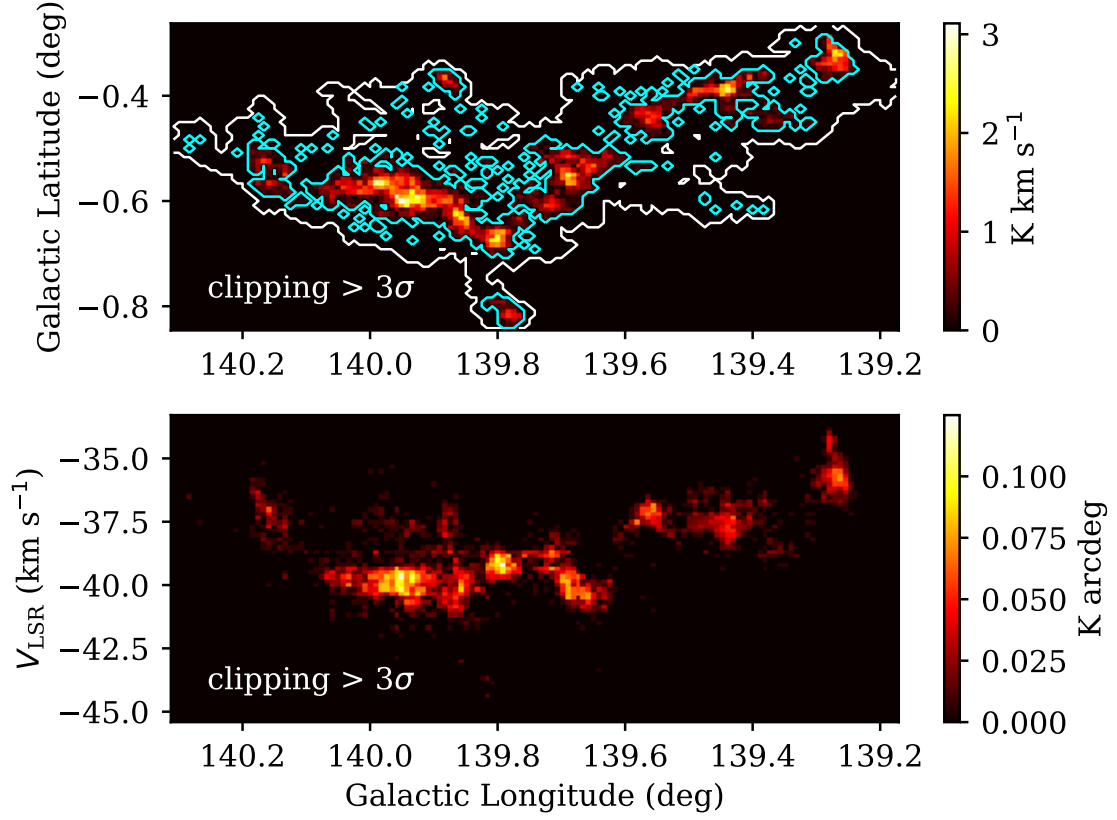


Figure C7. The velocity-integrated intensity map (**upper**) and latitude-integrated intensity map (**lower**) of ^{13}CO emission extracted within the ^{12}CO cloud G139.73 using the clipping at the cutoff level of 3σ (0.81 K). The white contours are the boundaries of ^{12}CO molecular cloud. The cyan contours are the determined boundaries of ^{13}CO line emission.

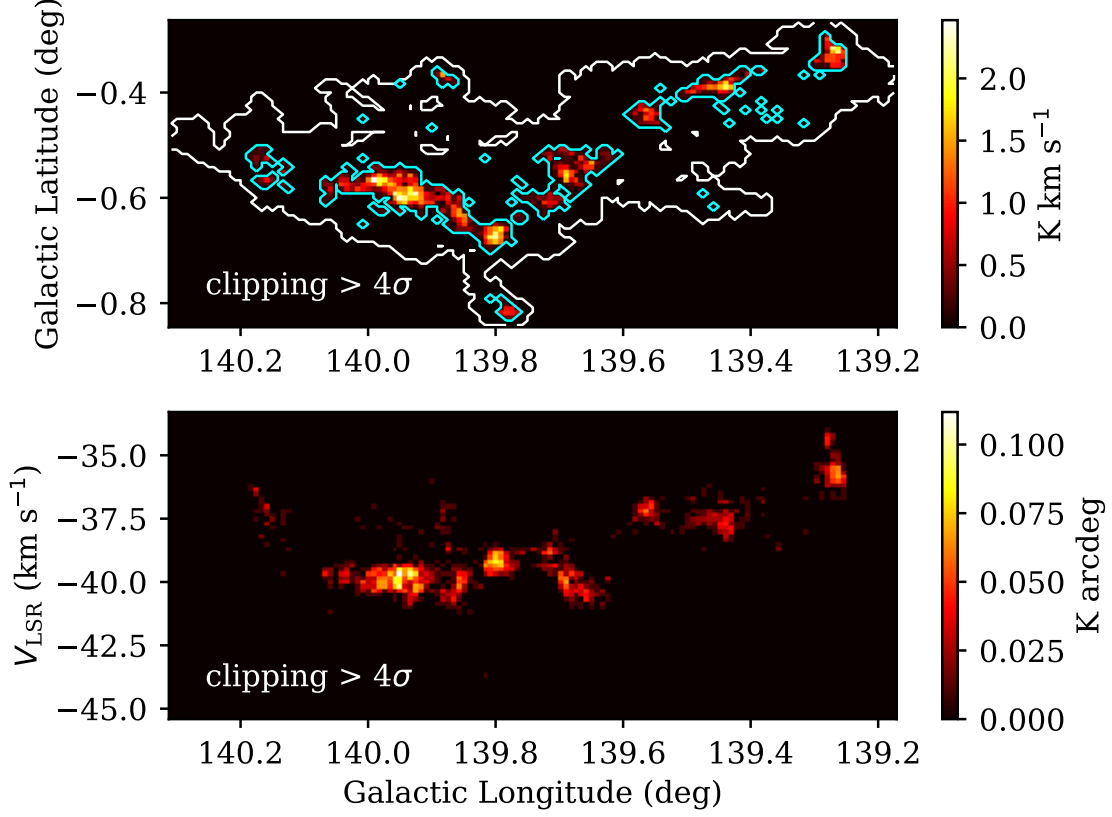


Figure C8. Same as Figure C7, but using the clipping at the cutoff level of 4σ (1.08 K).

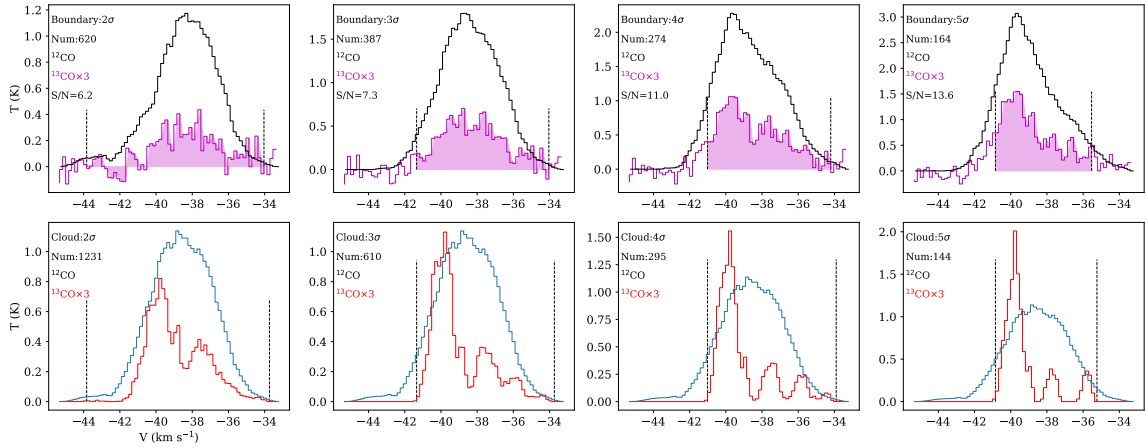


Figure C9. Same as Figure C6, but for the ^{13}CO structures extracted by the DBSCAN algorithm at the cutoff level of 2σ , 3σ , 4σ , and 5σ .

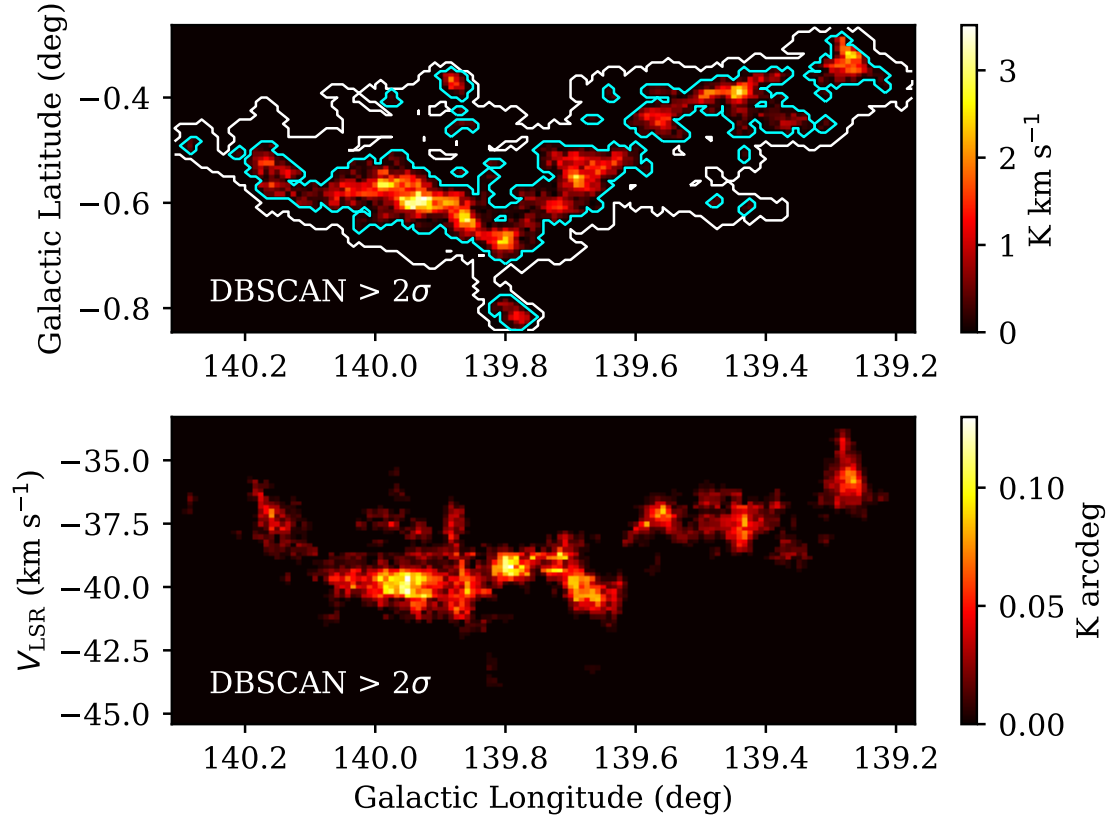


Figure C10. Same as Figure C7, but using the DBSCAN at the cutoff level of 2σ (0.54 K).

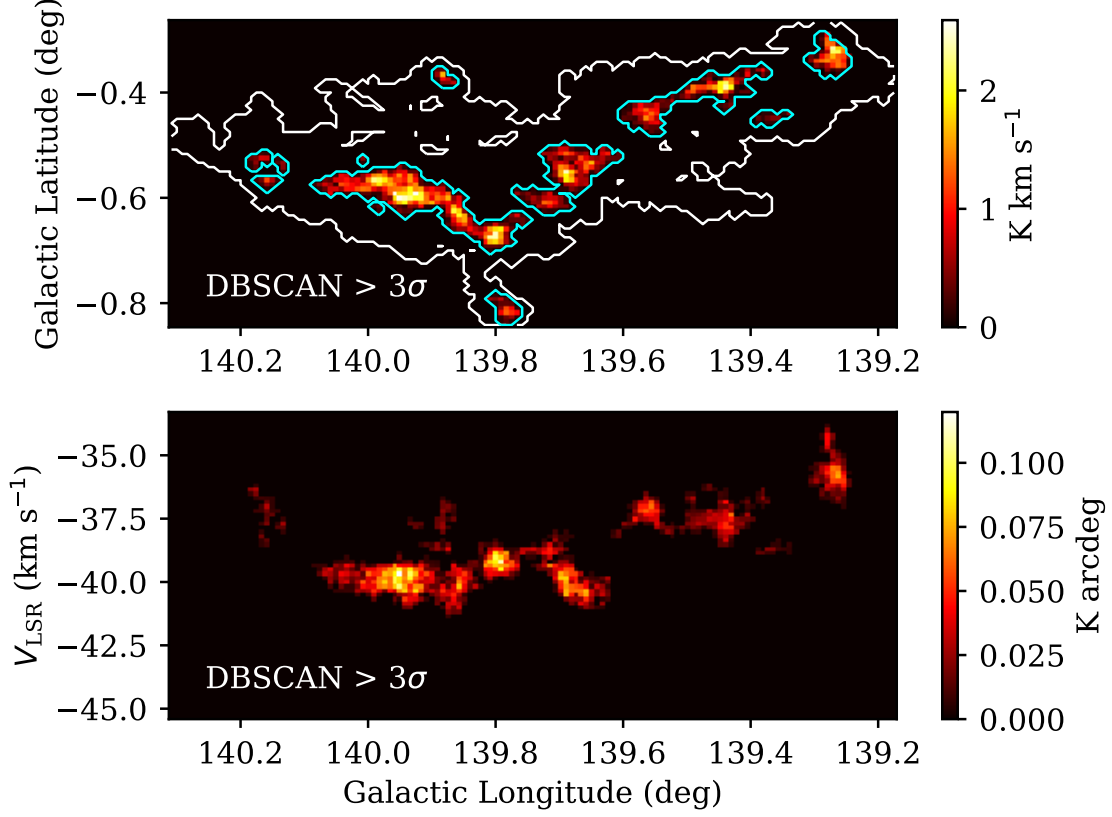


Figure C11. Same as Figure C7, but using the DBSCAN at the cutoff level of 3σ (0.81 K).

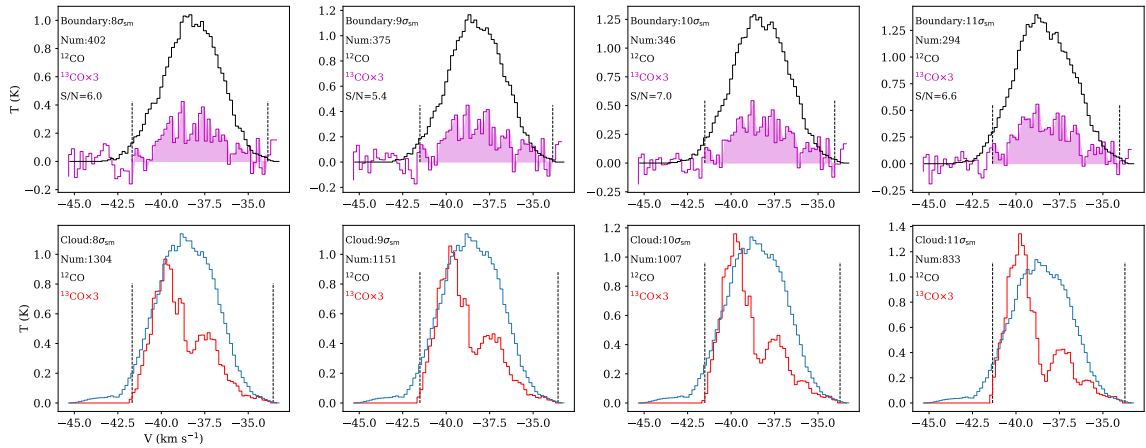


Figure C12. Same as Figure C6, but for the ^{13}CO structures identified by the moment mask at the cutoff level of $8\sigma_{\text{sm}}$, $9\sigma_{\text{sm}}$, $10\sigma_{\text{sm}}$ and $11\sigma_{\text{sm}}$. The noise σ_{sm} is calculated from the smoothed data. Its value is 0.05 K.

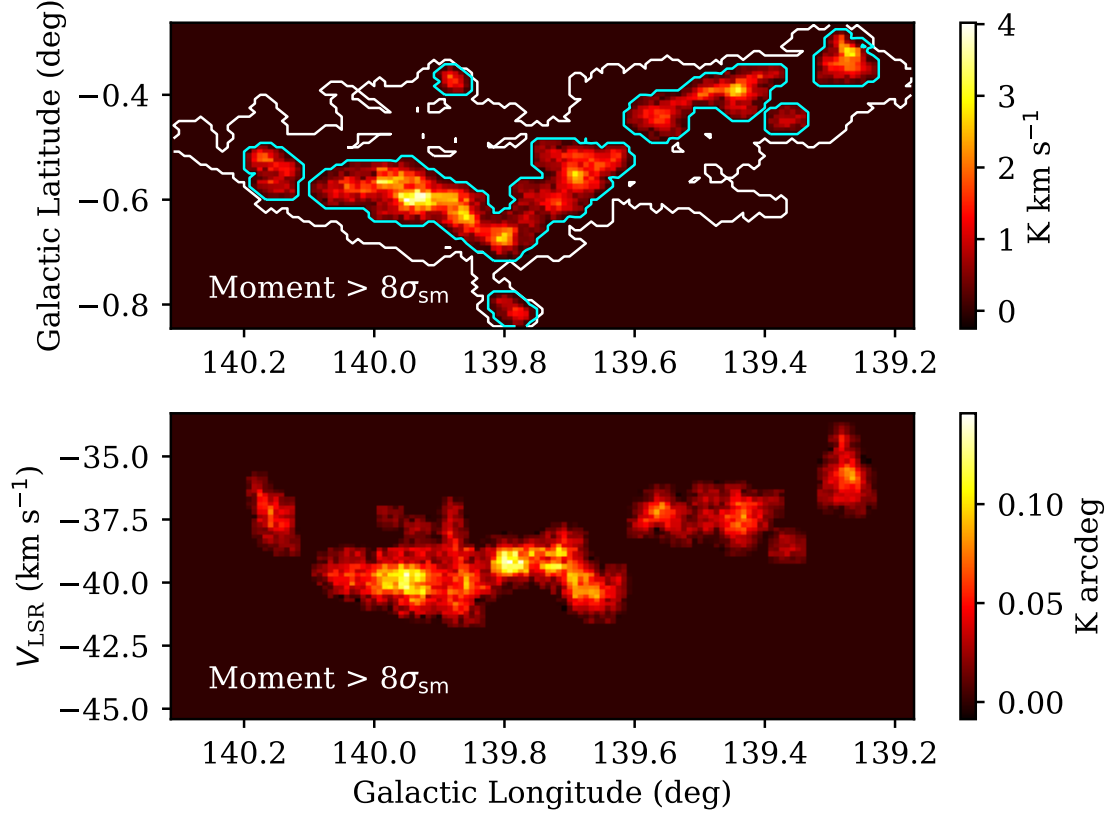


Figure C13. Same as Figure C7, but using the moment mask at the cutoff level of $8\sigma_{\text{sm}}$ (0.4 K).

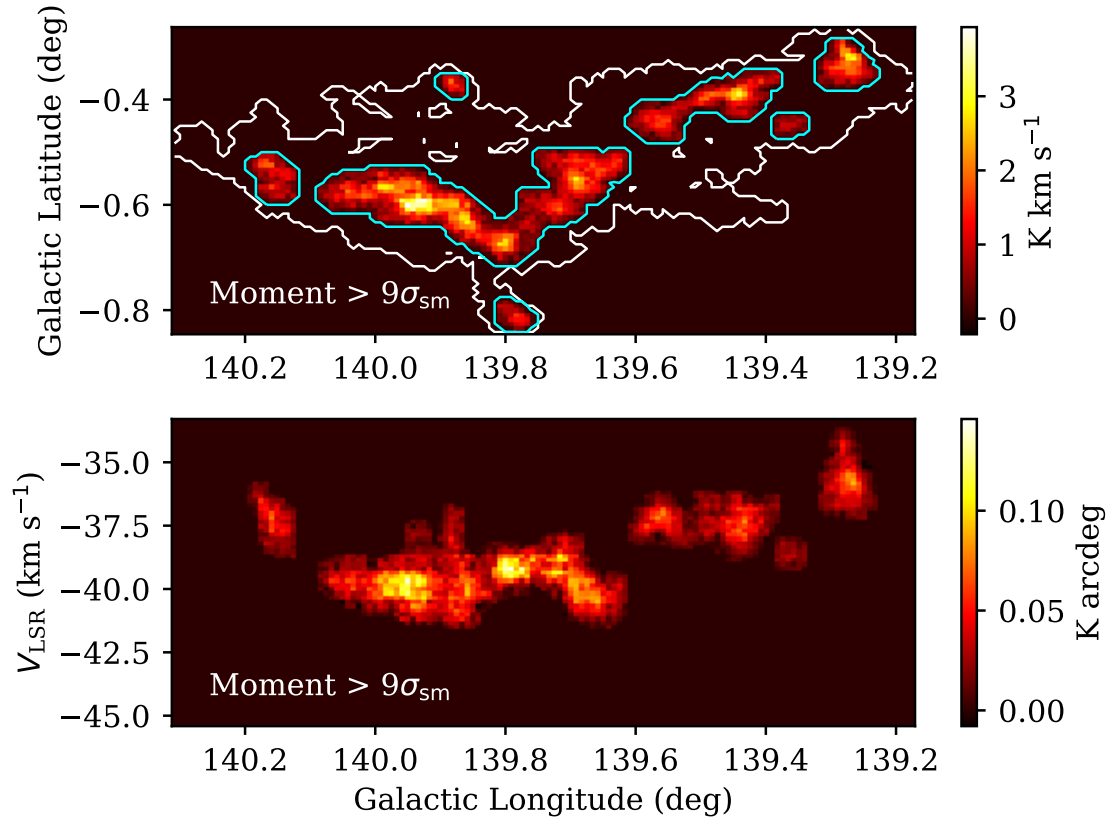


Figure C14. Same as Figure C7, but using the moment mask at the cutoff level of $9\sigma_{\text{sm}}$ (0.45 K).

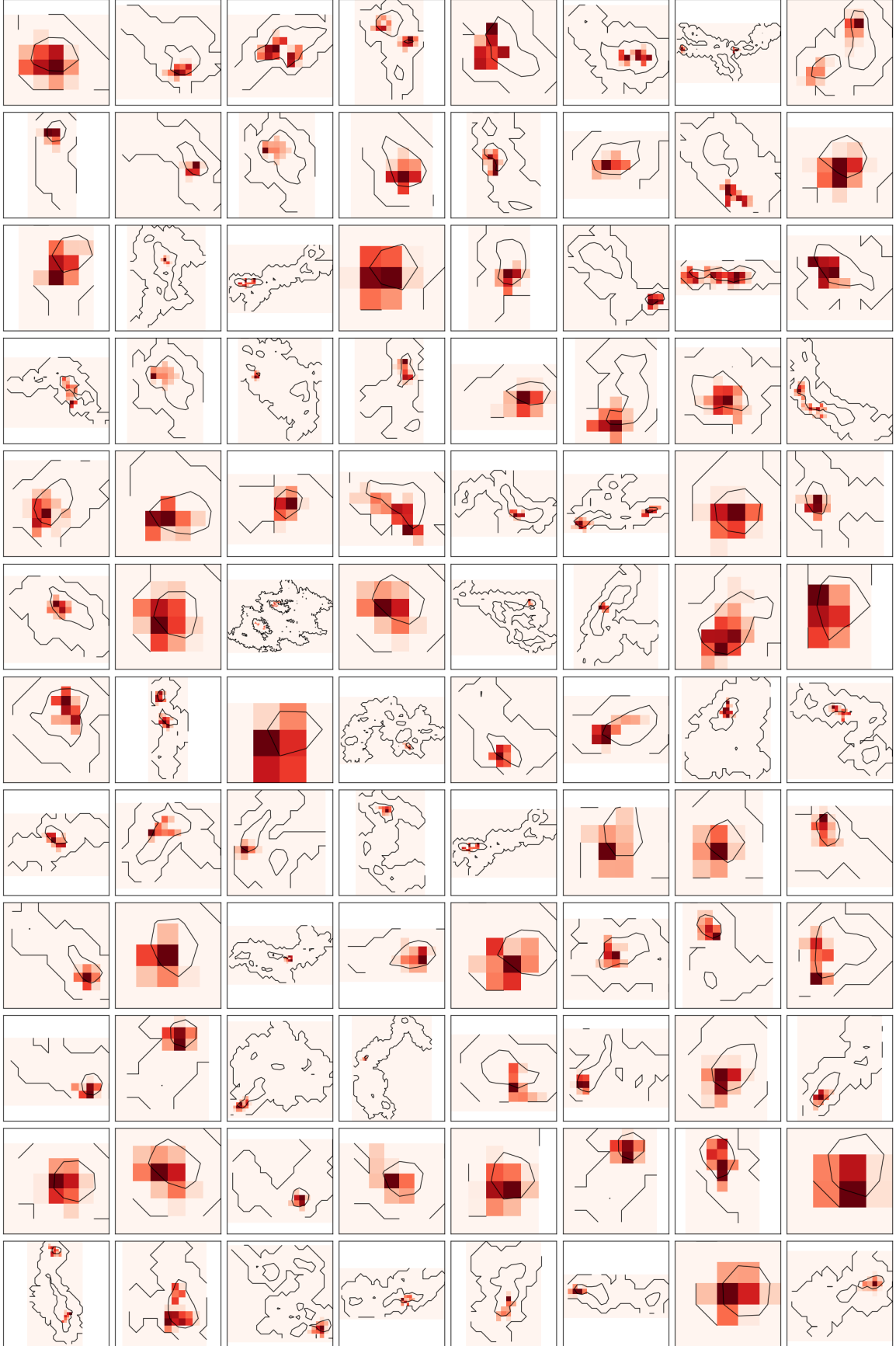


Figure D15. ^{13}CO structures identified by the DBSCAN, but not by the moment mask. The colormaps represent the distributions of the velocity-integrated intensities of ^{13}CO line emission. The black contours indicate the boundaries and the level of 50% at the ^{12}CO line velocity-integrated intensities.

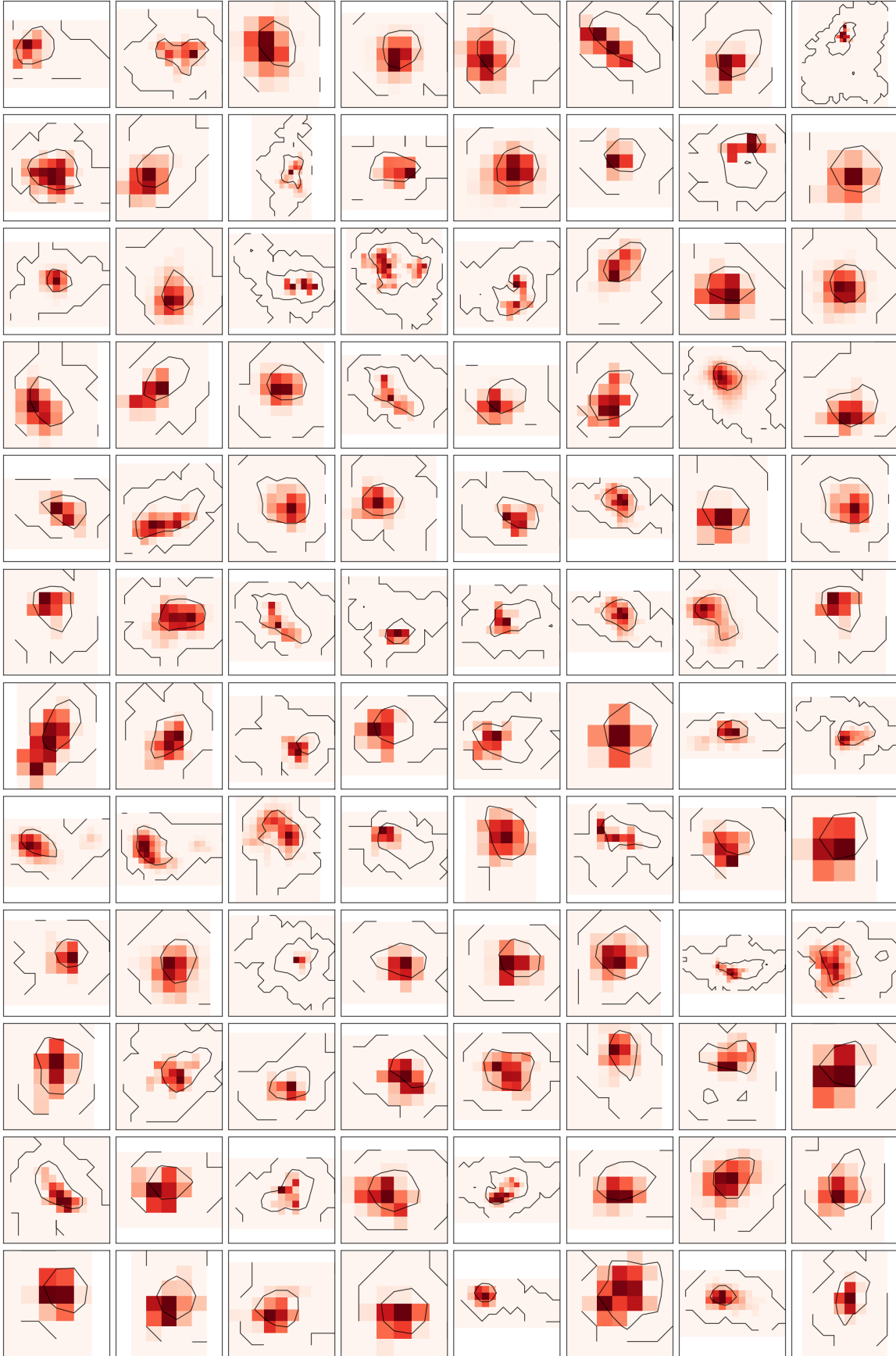


Figure D16. ^{13}CO structures identified by the DBSCAN. The colormaps represent the distributions of the velocity-integrated intensities of ^{13}CO line emission. The black contours indicate the boundaries and the level of 50% at the ^{12}CO line velocity-integrated intensities.

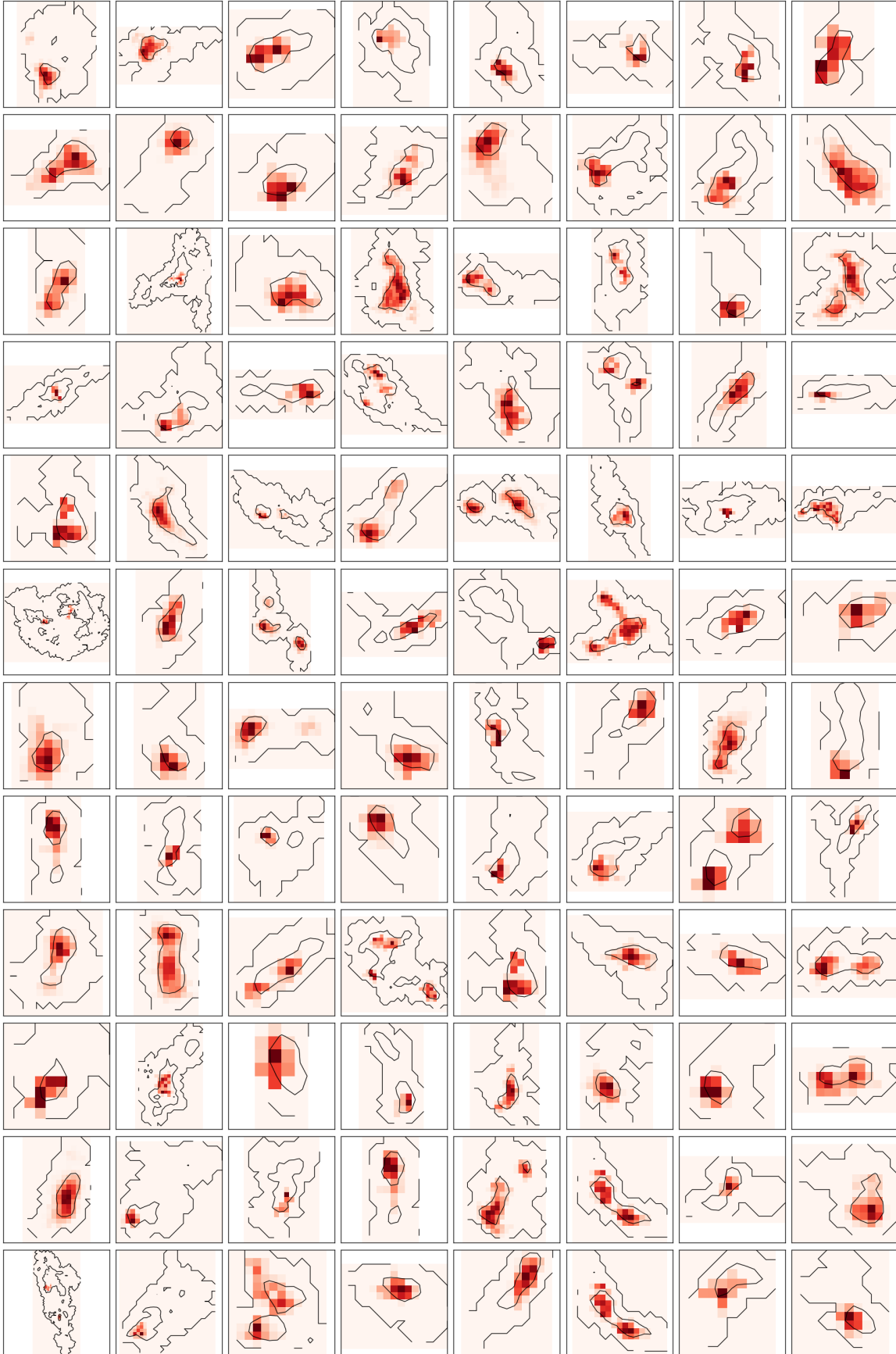


Figure D17. Same as above.

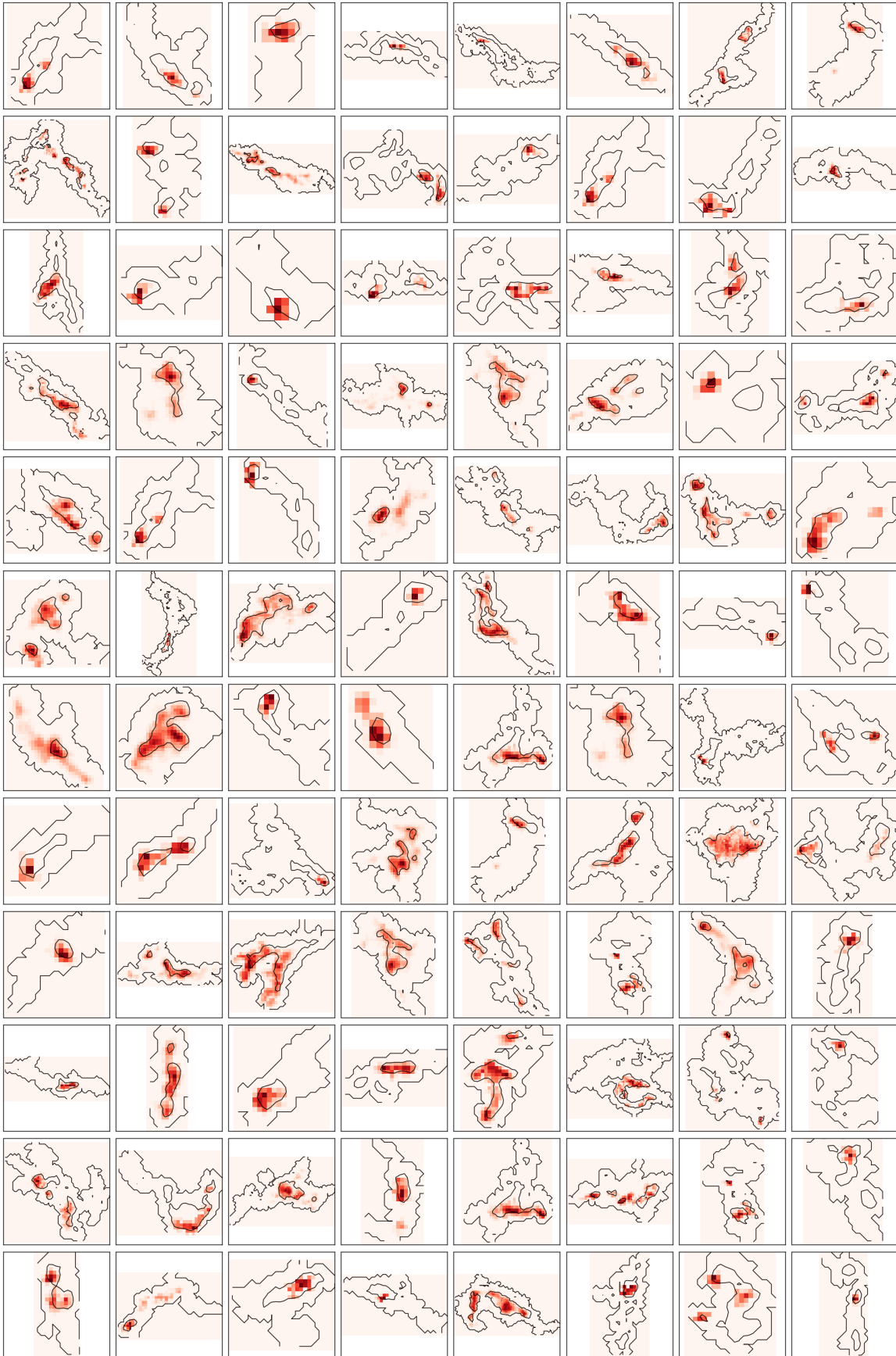


Figure D18. Same as above.

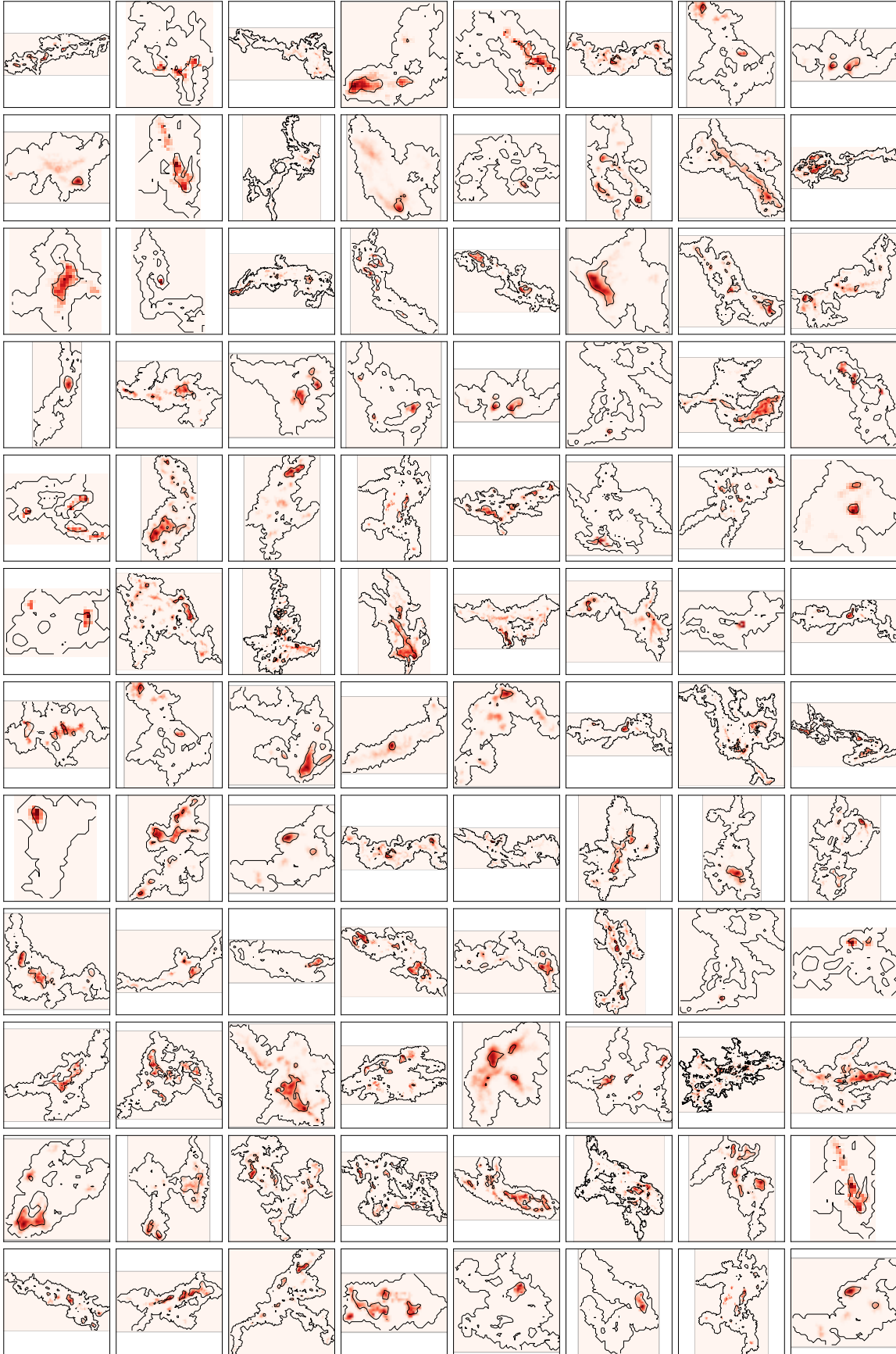


Figure D19. Same as above.

REFERENCES

- Abe, D., Inoue, T., Inutsuka, S.-i., & Matsumoto, T. 2021, *ApJ*, 916, 83, doi: [10.3847/1538-4357/ac07a1](https://doi.org/10.3847/1538-4357/ac07a1)
- André, P., Di Francesco, J., Ward-Thompson, D., et al. 2014, in *Protostars and Planets VI*, ed. H. Beuther, R. S. Klessen, C. P. Dullemond, & T. Henning, 27, doi: [10.2458/azu_uapress.9780816531240-ch002](https://doi.org/10.2458/azu_uapress.9780816531240-ch002)
- André, P., Men'shchikov, A., Bontemps, S., et al. 2010, *A&A*, 518, L102, doi: [10.1051/0004-6361/201014666](https://doi.org/10.1051/0004-6361/201014666)
- André, P., Revéret, V., Könyves, V., et al. 2016, *A&A*, 592, A54, doi: [10.1051/0004-6361/201628378](https://doi.org/10.1051/0004-6361/201628378)
- Arzoumanian, D., André, P., Peretto, N., & Könyves, V. 2013, *A&A*, 553, A119, doi: [10.1051/0004-6361/201220822](https://doi.org/10.1051/0004-6361/201220822)
- Arzoumanian, D., Shimajiri, Y., Inutsuka, S.-i., Inoue, T., & Tachihara, K. 2018, *PASJ*, 70, 96, doi: [10.1093/pasj/psy095](https://doi.org/10.1093/pasj/psy095)
- Arzoumanian, D., Russell, D., Zavagno, A., et al. 2022, *arXiv e-prints*, arXiv:2201.04267. <https://arxiv.org/abs/2201.04267>
- Astropy Collaboration, Robitaille, T. P., Tollerud, E. J., et al. 2013, *A&A*, 558, A33, doi: [10.1051/0004-6361/201322068](https://doi.org/10.1051/0004-6361/201322068)
- Astropy Collaboration, Price-Whelan, A. M., Sipőcz, B. M., et al. 2018, *AJ*, 156, 123, doi: [10.3847/1538-3881/aabc4f](https://doi.org/10.3847/1538-3881/aabc4f)
- Ballesteros-Paredes, J., Vázquez-Semadeni, E., & Scalo, J. 1999a, *ApJ*, 515, 286, doi: [10.1086/307007](https://doi.org/10.1086/307007)
- . 1999b, *ApJ*, 515, 286, doi: [10.1086/307007](https://doi.org/10.1086/307007)
- Beuther, H., Wang, Y., Soler, J., et al. 2020, *A&A*, 638, A44, doi: [10.1051/0004-6361/202037950](https://doi.org/10.1051/0004-6361/202037950)
- Bolatto, A. D., Wolfire, M., & Leroy, A. K. 2013, *ARA&A*, 51, 207, doi: [10.1146/annurev-astro-082812-140944](https://doi.org/10.1146/annurev-astro-082812-140944)
- Cormier, D., Bigiel, F., Jiménez-Donaire, M. J., et al. 2018, *MNRAS*, 475, 3909, doi: [10.1093/mnras/sty059](https://doi.org/10.1093/mnras/sty059)
- Dame, T. M. 2011, *arXiv e-prints*, arXiv:1101.1499. <https://arxiv.org/abs/1101.1499>
- Dobbs, C., & Baba, J. 2014, *PASA*, 31, e035, doi: [10.1017/pasa.2014.31](https://doi.org/10.1017/pasa.2014.31)
- Ester, M., Krieger, H.-P., Sander, J., & Xu, X. 1996, in *Proceedings of the Second International Conference on Knowledge Discovery and Data Mining, KDD'96 (AAAI Press)*, 226–231. <http://dl.acm.org/citation.cfm?id=3001460.3001507>
- Field, G. B., & Saslaw, W. C. 1965, *ApJ*, 142, 568, doi: [10.1086/148318](https://doi.org/10.1086/148318)
- Gallagher, M. J., Leroy, A. K., Bigiel, F., et al. 2018, *ApJ*, 858, 90, doi: [10.3847/1538-4357/aabad8](https://doi.org/10.3847/1538-4357/aabad8)
- Goldreich, P., & Lynden-Bell, D. 1965, *MNRAS*, 130, 97, doi: [10.1093/mnras/130.2.97](https://doi.org/10.1093/mnras/130.2.97)
- Gong, Y., Belloche, A., Du, F. J., et al. 2021, *A&A*, 646, A170, doi: [10.1051/0004-6361/202039465](https://doi.org/10.1051/0004-6361/202039465)
- Gratier, P., Pety, J., Bron, E., et al. 2021, *A&A*, 645, A27, doi: [10.1051/0004-6361/202037871](https://doi.org/10.1051/0004-6361/202037871)
- Hacar, A., & Tafalla, M. 2011, *A&A*, 533, A34, doi: [10.1051/0004-6361/201117039](https://doi.org/10.1051/0004-6361/201117039)
- Heitsch, F., Slyz, A. D., Devriendt, J. E. G., Hartmann, L. W., & Burkert, A. 2006, *ApJ*, 648, 1052, doi: [10.1086/505931](https://doi.org/10.1086/505931)
- Henshaw, J. D., Caselli, P., Fontani, F., et al. 2016, *MNRAS*, 463, 146, doi: [10.1093/mnras/stw1794](https://doi.org/10.1093/mnras/stw1794)
- Heyer, M., & Dame, T. M. 2015, *ARA&A*, 53, 583, doi: [10.1146/annurev-astro-082214-122324](https://doi.org/10.1146/annurev-astro-082214-122324)
- Hunter, J. D. 2007, *Computing in Science & Engineering*, 9, 90, doi: [10.1109/MCSE.2007.55](https://doi.org/10.1109/MCSE.2007.55)
- Inoue, T., & Fukui, Y. 2013, *ApJL*, 774, L31, doi: [10.1088/2041-8205/774/2/L31](https://doi.org/10.1088/2041-8205/774/2/L31)
- Inoue, T., Hennebelle, P., Fukui, Y., et al. 2018, *PASJ*, 70, S53, doi: [10.1093/pasj/psx089](https://doi.org/10.1093/pasj/psx089)
- Kainulainen, J., Stutz, A. M., Stanke, T., et al. 2017, *A&A*, 600, A141, doi: [10.1051/0004-6361/201628481](https://doi.org/10.1051/0004-6361/201628481)
- Koyama, H., & Inutsuka, S.-i. 2002, *ApJL*, 564, L97, doi: [10.1086/338978](https://doi.org/10.1086/338978)
- Kwan, J., & Valdes, F. 1983, *ApJ*, 271, 604, doi: [10.1086/161227](https://doi.org/10.1086/161227)
- Lin, C. C., & Shu, F. H. 1964, *ApJ*, 140, 646, doi: [10.1086/147955](https://doi.org/10.1086/147955)
- Lin, Y., Csengeri, T., Wyrowski, F., et al. 2019, *A&A*, 631, A72, doi: [10.1051/0004-6361/201935410](https://doi.org/10.1051/0004-6361/201935410)
- Lu, X., Zhang, Q., Liu, H. B., et al. 2018, *ApJ*, 855, 9, doi: [10.3847/1538-4357/aaad11](https://doi.org/10.3847/1538-4357/aaad11)
- Matsumoto, T., Dobashi, K., & Shimoikura, T. 2015, *ApJ*, 801, 77, doi: [10.1088/0004-637X/801/2/77](https://doi.org/10.1088/0004-637X/801/2/77)
- Méndez-Hernández, H., Ibar, E., Knudsen, K. K., et al. 2020, *MNRAS*, 497, 2771, doi: [10.1093/mnras/staa1964](https://doi.org/10.1093/mnras/staa1964)
- Molinari, S., Swinyard, B., Bally, J., et al. 2010, *A&A*, 518, L100, doi: [10.1051/0004-6361/201014659](https://doi.org/10.1051/0004-6361/201014659)
- Neralwar, K. R., Colombo, D., Duarte-Cabral, A., et al. 2022a, *arXiv e-prints*, arXiv:2203.02504. <https://arxiv.org/abs/2203.02504>
- . 2022b, *arXiv e-prints*, arXiv:2205.02253. <https://arxiv.org/abs/2205.02253>
- Oort, J. H. 1954, *BAN*, 12, 177
- Padoan, P., & Nordlund, Å. 1999, *ApJ*, 526, 279, doi: [10.1086/307956](https://doi.org/10.1086/307956)
- Passot, T., Vázquez-Semadeni, E., & Pouquet, A. 1995, *ApJ*, 455, 536, doi: [10.1086/176603](https://doi.org/10.1086/176603)

- Peretto, N., Adam, R., Ade, P., et al. 2022, in European Physical Journal Web of Conferences, Vol. 257, European Physical Journal Web of Conferences, 00037, doi: [10.1051/epjconf/202225700037](https://doi.org/10.1051/epjconf/202225700037)
- Pudritz, R. E., & Kevlahan, N. K. R. 2013, Philosophical Transactions of the Royal Society of London Series A, 371, 20120248, doi: [10.1098/rsta.2012.0248](https://doi.org/10.1098/rsta.2012.0248)
- Reid, M. J., Dame, T. M., Menten, K. M., & Brunthaler, A. 2016, ApJ, 823, 77, doi: [10.3847/0004-637X/823/2/77](https://doi.org/10.3847/0004-637X/823/2/77)
- Roberts, W. W. 1969, ApJ, 158, 123, doi: [10.1086/150177](https://doi.org/10.1086/150177)
- Roman-Duval, J., Heyer, M., Brunt, C. M., et al. 2016, ApJ, 818, 144, doi: [10.3847/0004-637X/818/2/144](https://doi.org/10.3847/0004-637X/818/2/144)
- Su, Y., Yang, J., Zhang, S., et al. 2019, ApJS, 240, 9, doi: [10.3847/1538-4365/aaf1c8](https://doi.org/10.3847/1538-4365/aaf1c8)
- Tasker, E. J., & Tan, J. C. 2009, ApJ, 700, 358, doi: [10.1088/0004-637X/700/1/358](https://doi.org/10.1088/0004-637X/700/1/358)
- Tokuda, K., Fukui, Y., Harada, R., et al. 2019, ApJ, 886, 15, doi: [10.3847/1538-4357/ab48ff](https://doi.org/10.3847/1538-4357/ab48ff)
- Tomisaka, K. 1984, PASJ, 36, 457
- Torii, K., Fujita, S., Nishimura, A., et al. 2019, PASJ, 71, S2, doi: [10.1093/pasj/psz033](https://doi.org/10.1093/pasj/psz033)
- Vázquez-Semadeni, E., Passot, T., & Pouquet, A. 1995, ApJ, 441, 702, doi: [10.1086/175393](https://doi.org/10.1086/175393)
- Vázquez-Semadeni, E., Ryu, D., Passot, T., González, R. F., & Gazol, A. 2006, ApJ, 643, 245, doi: [10.1086/502710](https://doi.org/10.1086/502710)
- Wilson, R. W., Jefferts, K. B., & Penzias, A. A. 1970, ApJL, 161, L43, doi: [10.1086/180567](https://doi.org/10.1086/180567)
- Yan, Q.-Z., Yang, J., Su, Y., Sun, Y., & Wang, C. 2020, ApJ, 898, 80, doi: [10.3847/1538-4357/ab9f9c](https://doi.org/10.3847/1538-4357/ab9f9c)
- Yan, Q.-Z., Yang, J., Sun, Y., et al. 2021, A&A, 645, A129, doi: [10.1051/0004-6361/202039768](https://doi.org/10.1051/0004-6361/202039768)
- Yuan, L., Yang, J., Du, F., & Su, Y. 2022, The ^{12}CO and ^{13}CO lines data of 18,190 molecular clouds from the MWISP CO survey, V1, Science Data Bank, doi: [10.57760/sciencedb.j00001.00427](https://doi.org/10.57760/sciencedb.j00001.00427)
- Yuan, L., Zhu, M., Liu, T., et al. 2019, MNRAS, 487, 1315, doi: [10.1093/mnras/stz1266](https://doi.org/10.1093/mnras/stz1266)
- Yuan, L., Li, G.-X., Zhu, M., et al. 2020, A&A, 637, A67, doi: [10.1051/0004-6361/201936625](https://doi.org/10.1051/0004-6361/201936625)
- Yuan, L., Yang, J., Du, F., et al. 2021, ApJS, 257, 51, doi: [10.3847/1538-4365/ac242a](https://doi.org/10.3847/1538-4365/ac242a)